The present work was submitted to the Institute of Crystallography

Title: Spin-Crossover in $[Fe(NQu_3)(NCS)_2]$: Structural and Magnetic Studies

Master Thesis

Presented by

Zhou, Wenling

Student ID no. 391739

1st examiner: apl. Prof. Dr. Karen Friese

2nd examiner: Priv.-Doz. Dr. Lars Peters

Aachen, 16.05.2025

Contents

Abstract

This thesis investigates the magnetic and structural properties of two batches of single crystals (freshly synthesized and aged) and polycrystalline material of the spin-crossover (SCO) compound $[Fe(NQu_3)(NCS)_2]\cdot 0.5\ Et_2O$ (Qu = quinoline and Et = ethyl). Magnetization measurements, carried out on in-house Superconducting Quantum Interference Device (SQUID) and on freshly synthesized single crystals, indicate that the compound exhibits abrupt SCO behaviour with a hysteresis width of 24.47 K. However, on freshly synthesized polycrystalline samples and on aged single crystals, only a paramagnetic signal was obtained across the entire temperature range (20-300 K) (measured on the Quantum Design Dynacool-PPMS (Physical Property Measurement System)), indicating the absence of a SCO. Based on these observations we believe that the particle size and the solvent molecules play a critical role in governing the SCO process.

The compound crystallizes in the symmetry *C2/c* (measured on in-house *SuperNova* single-crystal diffractometer), with the lattice parameters and volume at room temperature as a = 9.9054(2) Å, b = 22.3828(7) Å, c = 25.8754(8) Å, β = 95.5840(20)°, and V = 5709.63(45) $Å^3$. For both batches of single crystals, the symmetry was found to remain unchanged across the entire investigated temperature range (95-300 K). Based on the electron density map, the potential positions of the solvent molecules in freshly synthesized single crystals were identified. However, the electron density of solvent molecules at the same positions disappeared in aged single crystals.

The fresh samples show a SCO transition temperature ($T_{1/2}$) at 138 K in the cooling process and a temperature of 162.5 K in the warming process. The lattice parameters a and c, along with the angle β shrink significantly from HS to LS state, while the lattice parameter b expands. The FeN_6 octahedron contracts non-uniformly from HS to LS state, in which the Fe-N bonds are shortened by approximately 0.12 Å to 0.32 Å. Additionally, we observed a gradual increase in mosaicity when cooling down the crystal.

The results on the fresh crystals are compared and contrasted with the single crystal diffraction data of the "aged" single crystals, which do not exhibit a SCO transition, but instead show a smooth contraction of the unit cell volume with decreasing temperature. The compound $[Fe(NQu_3)(NCS)_2]\cdot 0.5\ Et_2O$ is an example of a spin crossover compound where the occurrence of the transition seems to be entirely governed by the concentration of solvent molecules. This serves as an excellent entry point for understanding and investigating the solvent-driven SCO phenomenon.

Acknowledgements

This is absolutely one of the most impressive and intensive six months in my life. I have been through so much work which I could not imagine before my master thesis started. And I know, it is very difficult to complete the work in time only with my effort. Therefore, my deep sense of gratitude goes to a list of names which I will mention below.

First of all, my appreciation goes to Prof. Dr. Karen Friese for providing me this opportunity to write my master thesis in her group in Quantum Materials and Collective Phenomena (JCNS-2), Jülich Centre for Neutron Science (JCNS), Forschungszentrum Jülich, and for squeezing her time to offer unwavering support when I had difficulties regarding my thesis. Furthermore, I would like to thank Dr. Lars Peters for agreeing to be my second examiner of my thesis.

Second, I extend my deepest gratitude to my supervisors: Dr. Hend Shahed and Dr. Pulkit Prakash for their invaluable guidance, expertise, and patience throughout this six months' time. Their insightful feedback, in-time response, and unconditional support shaped this work. Whenever I faced problems, they are always there, which I really appreciate it and feel lucky that Hend and Pulkit are my supervisors. Without their help, it is impossible for me to complete such amount of job in such limited time.

Third, I would like to thank the faculty and staff of JCNS, especially Prof. Dr. Manuel Angst, Mr. Jörg Perßon, Dr. Jörg Voigt and Mr. Berthold Schmitz, who always provide many scientific and technical supports when I faced problems in such as experiments, data processing, etc.

To my colleagues – Dr. Ji Qi, Mr. Chenyang Yin and Ms. Barbara Daegener – thank you for your patience of answering many my "silly" questions. My colleagues are always glad to help me to familiar how things work in the institute, which is very grateful.

Finally, I would like to thank everyone who contributed to this journey, directly or indirectly, visibly or invisibly. I could not have done this work without you.

1 Introduction

SCO is a phenomenon in which a material undergoes a change of spin state when perturbed by external stimulation such as temperature, pressure or photoexcitation (Gütlich & Goodwin, 2004). An important and emerging potential application of these compounds is in the field of caloric refrigeration. Caloric refrigeration is based on the caloric effect and refers to a phenomenon where a material undergoes a reversible entropy change when exposed to an external perturbation such as magnetic, electric, and mechanical field (Planes et. al., 2015). The search for new caloric materials, which can be utilized as refrigerants in the new generation of solid-state refrigerators with improved energy efficiency and less environmental impact, has gathered significant interest of the scientific community (von Ranke et. al., 2019). Apart from direct applications, research in this field is also driven from a fundamental material science perspective aiming at thermodynamics behind SCO, crystallographic investigation of SCO materials, etc. (Gütlich & Goodwin, 2004).

In this thesis we investigate the SCO compound $[Fe(NQu_3)(NCS)_2]$ (NQu_3 = tris(quinoline-8-yl)amine) from a magnetic and structural perspective. This compound was found to co-crystallize with the solvent diethyl ether ($(CH_3CH_2)_2O$) in previous investigations (H. M. Hüppe, PhD thesis, RWTH Aachen (2023)), with four molecules of diethyl ether present in each unit cell. However, the exact quantity and arrangement of these solvent molecules and their role in the SCO process is not well understood.

The magnetic properties of the compound are probed by the Superconducting Quantum Interference Device (SQUID) and the Quantum Design Dynacool-PPMS (Physical Property Measurement System) (see section 3.3) to determine the absence or presence of SCO phenomenon in the compounds. It became obvious from these measurements, that the presence or absence of a SCO transition depended on the age (and possible the concentration and arrangement of the solvent) of the crystals.

To understand the underlying reasons for this behaviour, single crystal diffraction experiments were performed on fresh and aged crystals structure using an in-house *SuperNova* single-crystal diffractometer (see section 3.4.1) and a single crystal diffractometer at the Swiss-Norwegian Beamlines at the ESRF (European Synchrotron Radiation Facility) (see section 3.4.2). On the basis of these data, the structural differences between freshly synthesized crystals and aged crystals were elucidated.

We list some key findings and strive to highlight the effect of solvent molecules in SCO compounds and the non-trivial role played by them in spin transition process.

1.1 The Spin-Crossover Phenomenon

The spin-crossover phenomenon was first discovered by Cambi and Szego in Fe(III) dithiocarbomates in 1931 (Gütlich, 2013). SCO materials have two spin states under an external stimulation: the high spin (HS) and the low spin (LS) state. In the HS state the distribution of all the electrons in the *d* orbitals following Hund's rule, whereas in the LS state electron pairing takes place, violating the Hund's rule (Nicolazzi & Bousseksou, 2018). The development and switch between these two spin states can be understood within the framework of ligand field theory (discussed later in section 2.1). Understanding the correlation between the spin state transition and the thermodynamic properties of these compounds is essential for developing caloric application-based devices (von Ranke et. al., 2019).

In most investigations (Gütlich & Goodwin, 2004), the SCO phenomenon was found to exist in transition metal complexes. However, SCO does not happen in all the transition metal complexes (Nicolazzi & Bousseksou, 2018), but only in the first row of transition metal ions in the periodic table, which possess the electronic configuration $3d^4$ – $3d^7$ (Gütlich, 2013).

The scientific community strives to synthesize SCO compounds with different compositions, with the aim to create materials which are better suited for applications. Nowadays, about 90% of the research is based on Fe(II) complexes surrounded with various ligands, such as $[Fe(PM\text{-}L)_2(NCS)_2]$ (Ksenofontov et. al., 1998). Most of the rest 10% of studies focus on other first-row transition metal such as Fe(III) complexes (van Koningsbruggen et. al., 2004) and Co(III) complexes (Kläui et. al., 1987).

1.2 Effect of Solvent in Spin-Crossover

Some SCO compounds exhibit the presence of a solvent molecule which co-crystallizes during the synthesis. Studies show that the structural and magnetic characteristics of such SCO compounds are not only decided by the octahedral transition metal complexes, but also depend critically on the solvent molecule (Fumanal et. al., 2017). Sun and co-workers found out (Sun et. al., 2018) that eight different co-crystallized solvent molecules in $[Fe(tpa)(NCSe)_2]$ (tpa = tris(2-pyridylmethyl)amine) compound change the molecular packing and the transition temperature of SCO. In other compounds, the existence of diethyl ether solvent molecules can cause a narrow hysteresis loop in SCO compounds (Fumanal et. al., 2017). Moreover, an aging effect varying the nature of the SCO transition has been observed in SCO compounds with co-crystallized ethanol molecules (Phonsri et. al., 2017). It was also observed that a change in the concentration of the solvent molecule could change the nature of SCO transition (Šalitroš, 2016). Thus, it is evident that the co-crystallized solvent molecules can affect the structural and magnetic properties of SCO compounds significantly.

1.3 The SCO Compound $Fe(NQu_3)(NCS)_2 \cdot 0.5\ Et_2O$

In the compound investigated in this thesis, $Fe(NQu_3)(NCS)_2 \cdot 0.5Et_2O$, the Fe(II) ion is surrounded by six nitrogen atoms, forming an octahedral complex (see figure 1). Three of the six nitrogen atoms come from three quinoline ligands, two from thiocyanate groups, one from an amine group.

According to the previous information (Hüppe, 2023), the compound possesses a symmetry of *C2/c* at 200 K. The solvent molecules, however, are located between the $Fe(NQu_3)(NCS)_2$ molecules in a very disordered way and therefore could not be modelled in an adequate manner. After using the BYPASS algorithm implemented in SQUEEZE/PLATON (van der Sluis & Spek, 1990), there are 174 residual electrons in each unit cell despite the complex molecules, corresponding approximately 0.5 Et_2O molecules per complex molecule. Since this compound is a new SCO complex, its structural and magnetic properties have not been previously investigated in-depth, the work in this thesis focuses on investigating the magnetic behaviour and crystal structure under varying temperature.

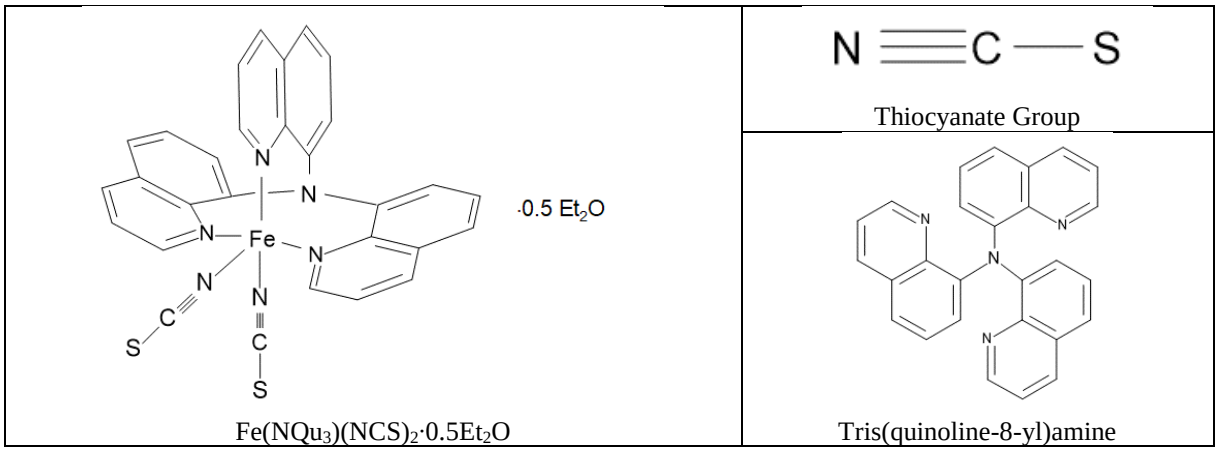

Figure 1: Illustration of the molecular unit in $Fe(NQu_3)(NCS)_2 \cdot 0.5Et_2O$

According to previous work (Hüppe, 2023), many compounds with quinoline as ligands, often co-crystallize with solvent molecules, for instance, $Fe(NQu_3)(OTf)_2 \cdot 0.45\ Et_2O$ (OTf = trifluoromethanesulfonate), $Fe(NQu_3)(MeCN)_2(BF_4)_2 \cdot 0.5$ MeCN (MeCN = methyl cyanide), and $Fe(NQu_3)Cl_2 \cdot 0.5$ DCM (DCM = dichloromethane). The solvent molecules which co-crystallize with the complex differ depending on the synthesis environment and counterions. Among the various complexes with $[Fe(NQu_3)]$ ligands, the compound $Fe(NQu_3)(NCS)_2 \cdot 0.5Et_2O$ investigated here is the most stable one when kept isolated from its synthesis environment (Hüppe, 2023).

Although there are not many Fe(II) compounds with a quinoline ligand, many works involve Fe(II) complexes with two thiocyanate groups. For example, in the $Fe(PM\text{-}L)_2(NCS)_2$ family (PM = N-(2'-pyridylmethylene); L = ligand forming aromatic sub-unit; Ksenofontov et. al. 1998), different family members show different natures of the SCO transition. Thus, $Fe(PM\text{-}A)_2(NCS)_2$ (A = aniline) has a step-like transition, while $Fe(PM\text{-}AzA)_2(NCS)_2$ (AzA = 4-(azophenyl)aniline) has a gradual transition and $Fe(PM\text{-}PEA)_2(NCS)_2$ (PEA = 4-(phenylethylnyl)aniline) shows an abrupt transition with wide hysteresis. In $Fe(PM\text{-}BiA)_2(NCS)_2$ (BiA = 4-(aminobiphenyl)aniline) where two polymorphs are observed, the orthorhombic polymorph shows an abrupt transition with narrow hysteresis and the monoclinic polymorph shows a gradual transition.

Although the compound $Fe(NQu_3)(NCS)_2 \cdot 0.5Et_2O$ may behave quite differently from the compounds in the literature, because it is new and remains unexplored, some features should be referable. For the SCO compound mentioned above, the lattice parameters and unit cell volumes in LS state are usually smaller than the ones in HS state, which is a consequence of

the shortening of the Fe-N distances at the SCO transition (Marchivie et. al., 2003 and Guionneau et. al., 1999).

This thesis serves as an initial step in understanding the SCO behaviour of the compound $Fe(NQu_3)(NCS)_2 \cdot 0.5Et_2O$. The magnetic and crystallographic properties of the compound are thoroughly investigated. The key findings, along with discussion on the results, and potential direction for future work will be summarized.

2 Theoretical Background

This chapter presents a brief description of the theoretical background needed to understand and interpret the work carried out in this thesis. The theoretical part lays the foundations for the experiments and discussions that follow in the remaining chapters of the thesis. The chapter is briefly divided into three sections, with the theories related to (i) the SCO effect, (ii) magnetism and (iii) crystal structure solution.

2.1 Crystal Field Theory and Ligand Field Theory

Since spin-crossover phenomenon is primarily associated with the arrangement of electrons in the *d*-orbitals (Gütlich, 2013), it is important to understand the theory that describes the effect of the neighboring atoms on these orbitals and the corresponding energy split.

Crystal field theory (CFT) is a chemical bonding model which describes how a transition metal ion interacts with the neighboring negative charges (Burns, 1993). Compared with the ligand field theory, in CFT, the negative charges are regarded as a point or a dipole. Although it is not the most accurate model and it fails at explaining particle interactions in some compound like e. g. in tris(aminoacidato)cobalt(III) complexes (Urland & Nektic, 1986), it is still very effective to explain many properties of transition metal elements.

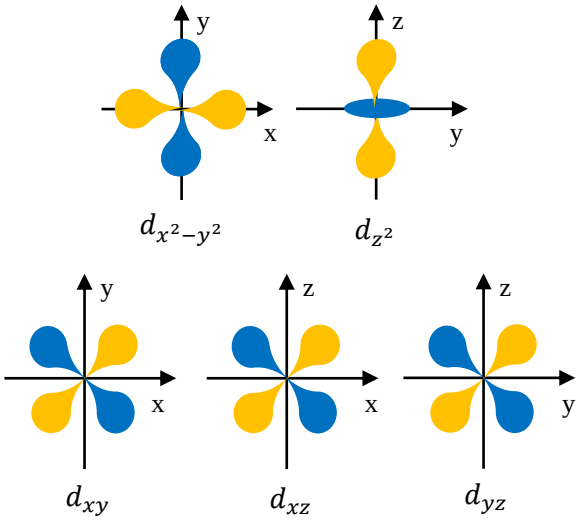

Figure 2: The configuration of *d* orbitals (figure after Weller et. al., 2014)

From quantum mechanics, it is well known that there are five *d* orbitals, namely the d_{xy}, d_{xz}, d_{yz}, d_{z^2}, and $d_{x^2-y^2}$, which for an isolated atom remain degenerate. An illustration of their configuration is shown in figure 2.

When the ion is placed in an octahedral complex where the negative charges are located at the vertices of the octahedron, the electron clouds of the *d* orbitals associated with the centre iron ion repulse with the negative charges at the vertices. As shown in figure 2, the geometry of the octahedral coordination environment influences the splitting of the metal *d* orbitals due to variations in electrostatic repulsion. The d_{z^2} and $d_{x^2-y^2}$ orbitals experience more repulsion from ligand electrons positioned at the vertices of the octahedron, whereas d_{xy}, d_{xz}, and d_{yz} orbitals experience relatively less repulsion. Consequently, the *d* orbitals split into two different energy levels. In the octahedral case (symmetry of O_h), the two energy levels are designated as E_g and T_{2g} (Douglas et al., 1985). Two of the *d* orbitals (d_{z^2} and $d_{x^2-y^2}$) are raised to E_g level and three orbitals (d_{xy}, d_{xz}, and d_{yz}) are lowered to T_{2g} level (Nicolazzi & Bousseksou, 2018; see figure 3).

The ligand field theory (LFT), however, specifies the splitting energy for the 3*d* orbitals. The magnitude of splitting energy can be described by the empirical parameter *Dq* using the expression:

$$Dq = \frac{1}{6}\frac{Ze^2}{a^5}\langle r^4 \rangle$$

Where *Z* represents the charge of the central ion; *e* is the electron charge; a is the metal-ligand distance; and *r* refers to the mean radius of the *d*-electron clouds (Douglas et al., 1985).

According to the orbital splitting mentioned above, three of the *d* orbitals decrease in energy to T_{2g} and two of them increase to E_g. Therefore, the ratio of the splitting E_g/T_{2g} is 3/2. If we assume that the total crystal field splitting energy in a Fe(II) octahedron complex is 10 Dq, then the E_g level is raised by 6 Dq and T_{2g} level is lowered by 4 Dq (see figure 3).

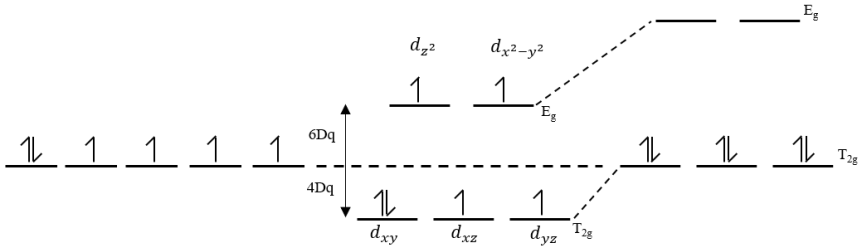

Figure 3: Splitting of d^6 orbital (figure after Douglas et al., 1985)

In the compound studied in this thesis, the central Fe^{2+} ($3d^6$) ion is present in an octahedral environment comprised of N^- ions. The 3-*d* electrons present in the *d* orbitals of the Fe^{2+} are distributed such that each of T_{2g} orbital receives one electron before any pairing occurs (Hund's rule). The last electron then fills one of the T_{2g} level (Pauli's rule), leading to a total four unpaired electrons, as shown in figure 3. The presence of unpaired electrons causes an effective spin of S=2 defining the state as the high spin state.

However, the substance is not always in high spin state, as the arrangement of electrons in *d*-orbitals is determined by whether the crystal field splitting energy (Δ) is greater or less than electron pairing energy (Π). In the high spin case, the value of Δ is smaller than Π (18 kK for Fe^{2+} (Douglas et al., 1985)). In cases where Π < Δ, the splitting of E_g and T_{2g} is so large that it costs much more energy to place electrons on orbitals at E_g level than to pair the electrons at T_{2g} level (Douglas et al., 1985). This leads to the absence of any unpaired electrons in the compound, giving S=0 or the so-called low spin state. In this case, Hund's rule no longer determines the electron arrangement. In compounds with $\Pi \approx \Delta$, the spin state becomes sensitive to external factors such as temperature (T) and pressure (P), allowing for a reversible transition between the high-spin and low-spin states (Nicolazzi & Bousseksou, 2018).

2.2 Thermodynamic aspect of SCO

The Gibbs free energy (*G*) is a thermodynamic potential energy which is expressed by the following equation:

$$G = U + PV - TS = H - TS \quad (2.1)$$

where *U*, *P*, *T* and *S* are internal energy, pressure, temperature and entropy, respectively (Cini, 2018).

The enthalpy is a thermodynamic quantity which is related to the internal energy *U*, the pressure *P* and the volume *V*. The enthalpy is expressed as:

$$H \equiv U + PV \quad (2.2)$$

According to the 2nd law of thermodynamics, the entropy change (*dS*) in a reversible process at temperature *T* is given by:

$$\frac{\delta Q}{T} = dS \quad (2.3)$$

where δQ is the heat change of the system and *dS* is the change in entropy.

From a thermodynamic point of view, the spin transition between LS and HS is driven by entropy (Nicolazzi & Bousseksou, 2018).

At equilibrium, *G* is constant; therefore, $\Delta G = 0$ (Equation 2.4). The critical temperature for the spin transition (where $\Delta G(T_{1/2}) \rightarrow 0$) is defined as the temperature where the number of molecules in the HS state is equal to the number of molecules in the LS state (figure 4). At this temperature, the pairing energy equals the crystal field splitting (Nicolazzi & Bousseksou, 2018).

$$\Delta G = \Delta H - T_{1/2} \cdot \Delta S = 0 \quad (2.4)$$

where $\Delta H = H_{HS}-H_{LS}$ and $\Delta S = S_{HS}-S_{LS}$ are the enthalpy and the entropy difference between the HS and LS states. Rearranging Equation 2.4 gives:

$$T_{1/2} = \frac{\Delta H}{\Delta S} \quad (2.5)$$

When $T < T_{1/2}$, the enthalpy plays a more important role. The system tends to stay in LS state. When $T > T_{1/2}$, the entropy term dominates, the system prefers to stay in the HS state (Nicolazzi & Bousseksou, 2018).

Usually, the variation of enthalpy as well as entropy can be subdivided. The difference in enthalpy can be divided to different contributions according to the following equation:

$$\Delta H = \Delta H_{el} + \Delta H_{vib} \quad (2.6)$$

where ΔH_{el} refers to electronic part and ΔH_{vib} represents the vibrational part. The entropy difference, however, is divided into four parts:

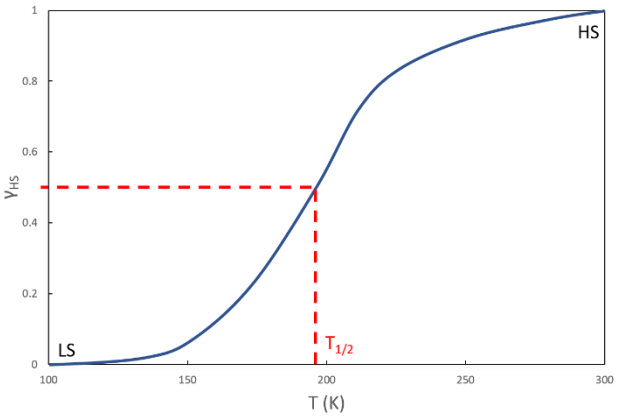

Figure 4: The temperature dependence of the spin-crossover phenomenon (figure after Nicolazzi & Bousseksou, 2018)

$$\Delta S = \Delta S_{el} + \Delta S_{vib} + \Delta S_{trans} + \Delta S_{rot} \quad (2.7)$$

where ΔS_{el} refers to electronic entropy; ΔS_{vib} represents the vibrational entropy; ΔS_{trans} is the translational entropy; and ΔS_{rot} is the rotational entropy. In the solid state, ΔS_{trans} and ΔS_{rot} can be neglected (Nicolazzi & Bousseksou, 2018). The vibrational entropy difference is temperature dependent. In the spin-crossover process, the vibrational entropy contributes to more than 70% of the total entropy change (Nicolazzi & Bousseksou, 2018).

2.3 The Nature of Spin-Crossover Transition

The nature of spin state transition varies across different materials and remains difficult to predict. There are several types of spin transition processes: gradual, abrupt, abrupt with a hysteresis, step-like, and an incomplete transition (figure 5).

The degree of cooperativity is the most important factor that influences the nature of the spin-crossover transition curve. When cooperativity is weak, a compound shows a gradual transition. When it is strong, however, a compound exhibits an abrupt transition (Vela & Paulsen, 2018).

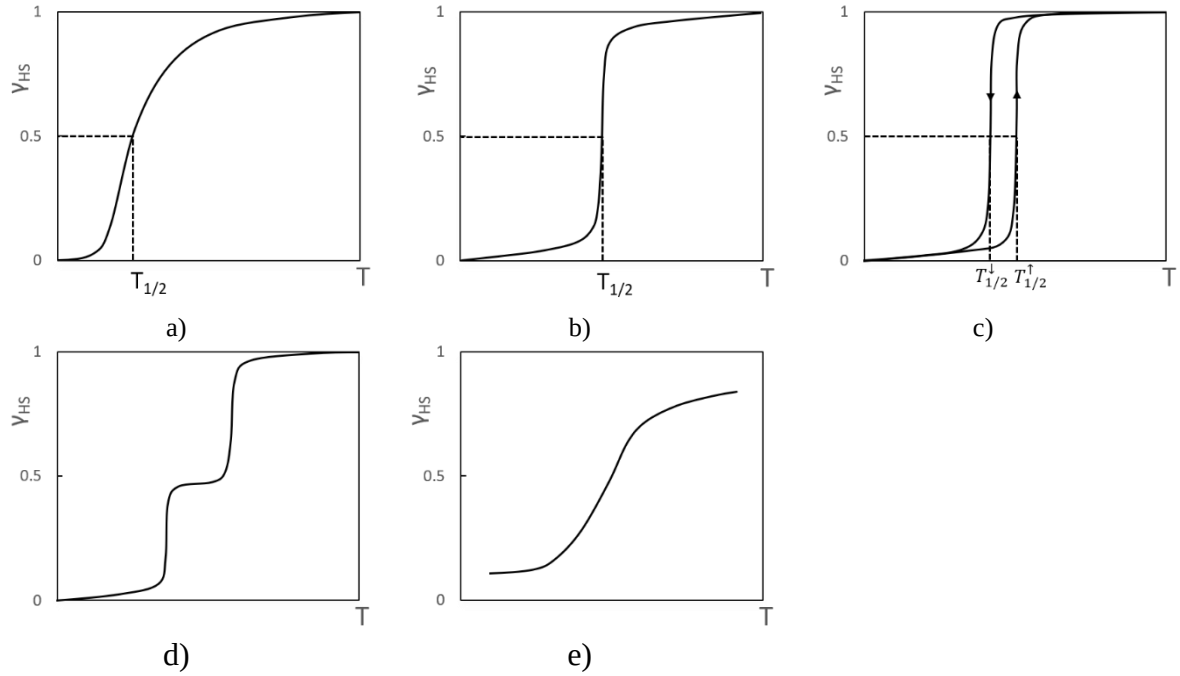

Figure 5: Different types of spin-crossover transition: a) gradual transition; b) abrupt transition; c) hysteresis transition; d) step-like transition; e) incomplete transition. (figure after Gütlich et. al., 2000)

In some materials, the transition shows a hysteresis loop which is a result of combined ligand field strength and cooperativity in the short and long range (Bousseksou et. al., 2003). This characteristic leads to a different $T_{1/2}$ during the warming or cooling process (Vela & Paulsen, 2018). The origin of hysteresis can be a crystallographic phase transition of the compound that happens together with the spin-crossover phenomenon or the intramolecular structural changes which affect the neighbouring molecules (Gütlich & Goodwin, 2004). Besides, the existence of solvent molecules that can, in some case, co-crystallize with compound molecules, could also drive a SCO transition with a hysteresis (Fumanal et. al., 2017).

2.4 Magnetism

2.4.1 Diamagnetism

Diamagnetism is a phenomenon, in which the magnetic dipoles are aligned opposite to the direction of an applied magnetic field. Diamagnetic materials do not possess permanent dipoles. If a diamagnetic material is placed in a homogeneous magnetic field, the flux density inside the material will decrease.

When the magnetic moments of all the electrons in the atoms are summed up, the susceptibility (χ) of diamagnetic material can be expressed as:

$$\chi = \frac{M}{H} = -\frac{\mu_0 Z e^2 N < r_0^2 >}{6m} \tag{2.8}$$

where M is the magnetization; H is the field strength; N is the number of atoms per m^3; μ_0 is the vacuum permeability; m is the mass of the electron; and $< r_0^2 >$ represents the average distance of the electron from the nucleus. This is Langevin's formula which refers to core electrons' volume susceptibility of diamagnetism (Pillai, 2006).

As Langevin's formula indicates, the larger the atomic number, the bigger the susceptibility value, as if the atomic number increases, the average distance of the electrons from the nucleus also increases. Furthermore, unlike paramagnetic materials, the susceptibility of diamagnetic materials does not depend on the temperature, because it is determined by the internal structure of the atom. All materials show diamagnetism, which originates from the response of the orbital momentum of the electrons to the applied external magnetic field (Kittel & McEuen, 2018).

2.4.2 Paramagnetism

Compared with diamagnetism, paramagnetism refers to the alignment of permanent magnetic dipoles in the field direction, if magnetic field is applied (Kittel & McEuen, 2018). In paramagnetic materials, unpaired electrons in the outermost shell are less tightly bound to the atomic core than the inner electrons. Therefore, the permanent magnetic dipoles in the material distribute their directions randomly due to thermal movement in the absence of an external magnetic field (Pillai, 2006).

In an applied field, if there is no thermal movement, the magnetic moments would turn fully towards the field direction, which would cause a huge magnetization. However, thermal movement tries to keep the randomization of the atomic dipole moments and competes with the force to align the magnetic moments due to the external magnetic field. Thus, only a partial alignment is reached which causes a weaker magnetization of paramagnetic materials (Pillai, 2006). Their susceptibilities are positive because they are magnetized in the same direction as the external field (Kittel & McEuen, 2018).

For paramagnetic materials, the equation of susceptibility is given as:

$$\chi = \frac{M}{H} = \frac{\mu_m^2 \mu_0 N}{3k_B\left(T - \frac{\mu_m^2 N \lambda}{3k_B}\right)} = \frac{\mu_m^2 \mu_0 N}{3k_B(T-\theta_C)} = \frac{C}{T-\theta_C} \tag{2.9}$$

where μ_m is the Bohr magneton; k_B is the Boltzmann constant, and $\theta_C = \frac{\mu_m^2 N \lambda}{3k_B}$ is called paramagnetic Curie temperature. This expression is also referred to as Curie-Weiss law (Pillai,

2006). Most of the paramagnetic materials have a positive but small susceptibility at room temperature (Kittel & McEuen, 2018).

2.5 Intermolecular Interactions

Intermolecular interactions play a vital role in governing the overall cooperativity and the nature of SCO in a compound. The existence of intermolecular interactions is due to the attractive and repulsive forces between molecules. There are van-der-Waals force (Hermann & Tkatchenko, 2017), hydrogen bridges (Grabowski, 2006), π-π interactions (Hunter & Sanders, 1990), London dispersion force (Liptrot & Power, 2017) etc. Some of these interactions, which play a non-trivial role in SCO, are van-der-Waals and π-π interactions and H bridges. From an energy perspective, the hydrogen bridges are the strongest among all of them. Then the van-der-Waals interaction follows, while the π-π interactions tend to be weaker than van-der-Waals interaction (Kato & Ishii, 2023).

Table 1: Energy range of intermolecular interactions (Kato & Ishii, 2023)

Interaction types	Energy range (k cal·mol^{-1})
Hydrogen bridge	25 – 48
Van-der-Waals interaction	10 – 30
π-π interaction	< 10

2.5.1 Hydrogen bridge

Hydrogen bridge is a dipole-dipole attraction between molecules. Since hydrogen has the lowest atomic number and only one electron, the non-uniform charge distribution of its electron cloud, when it is connected to other atoms, makes hydrogen a dipole (Sanderson, 2012). This can cause many interactions among molecules containing hydrogen. In general, there are three types of hydrogen bonds with corresponding potential energy namely, strong, intermediate and weak. The energy of weak hydrogen bonding is under 4 k cal·mol^{-1}; the medium one ranges from 4 k cal·mol^{-1} – 15 k cal·mol^{-1}; and the strong hydrogen bridge ranges from 15 k cal·mol^{-1} – 40 k cal·mol^{-1} (Bulusu & Desiraju, 2020).

Each atom has its atomic radii, namely the closest distance to a neighbourhood particle. The atomic radii depend on the radius of the atom as well as the bonding type (Muller, 2007). Hydrogen radii vary depending on how the hydrogen bridge is surrounded by other atoms. According to the values observed in single crystals, most of the hydrogen radii ranges from 1.2 Å to 2 Å (Jeffrey & Yeon, 1986).

2.5.2 Van-der-Waals interaction

The van-der-Waals force exists in most of cases when the distance between the atoms is 1 Å to 2 Å (Israelachvili, 1974). The cause of van-der-Waals force between molecules is the heterogeneous charge distribution of the electronic cloud. In terms of the energy levels, they range from 10 k cal·mol^{-1} – 30 k cal·mol^{-1} (Kato & Ishii, 2023). The van-der-Waals radii of some atoms such as hydrogen, carbon, nitrogen, oxygen and sulphur are 1.2 Å, 1.7 Å, 1.55 Å, 1.52 Å and 1.8 Å, respectively (Muller, 2007).

2.5.3 π-π interaction

When the *p* orbitals line up and overlap with each other, a π-bond is formed and the electron density merges above and under the plane (see figure 6). The stable π bonds can be formed between the main group elements boron, carbon, nitrogen, and oxygen (Jutzi, 1975). π-bonds are very common in aromatic compounds.

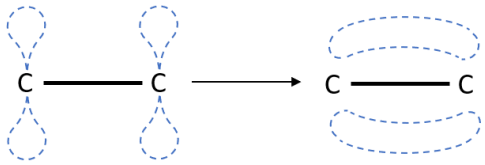

Figure 6: Overlap of *p* orbitals leading to π bond

The π-π interactions, however, are the interactions between one π-system to another π-system. Because of the overlap of π-orbitals, the electrons may have more possibilities to hop from one π-system to another. Thus, the π- π interactions have influence on energy bands, magnetism, etc. π-π interactions have strong geometrical requirements because the π-π interaction is usually a cooperative result of π-σ attractions and π-π repulsions in the compound (Hunter & Sanders, 1990). Therefore, the angles and alignment of each π system in the structure is critical for π- π interactions. The typical energy of a π-π bond is less than 10 k cal·mol^{-1}.

2.6 X-ray Diffraction

2.6.1 Form Factor and Structure Factor

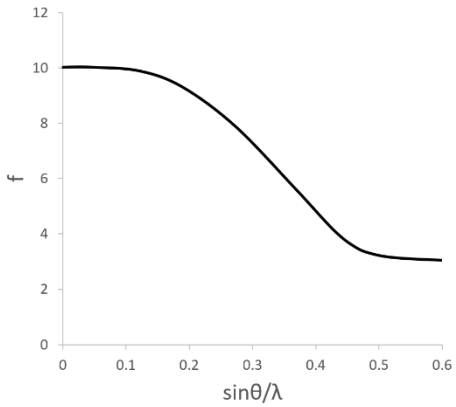

Figure 7: An illustrative diagram of form factor vs. sinθ/λ

The atomic form factor (f) is a parameter which describes how strong the X-rays are scattered by an atom. Mathematically, it is the Fourier transform of the atomic electron density distribution ρ (Schwarzenbach, 1996). The relationship between the form factor and sinθ/λ is illustrated in figure 7. Due to the effect of the form factor, the larger the scattering angle, the smaller the intensity of reflections (Schwarzenbach, 1996).

The structure factor (F_{hkl}) is a vector which describes the waves scattered by the atoms in a row of parallel lattice planes (hkl), giving rise to a reflection (hkl) in reciprocal space. F_{hkl} is related to the form factor of the atom and the phase information (Stout & Jensen, 1989). The expression of the structure factor is summed up by a real part and an imaginary part:

$$F_{hkl} = \sum f_i \cos 2\pi\left(hx_j + ky_j + lz_j\right) + i\sum f_i \sin 2\pi\left(hx_j + ky_j + lz_j\right) \quad (2.10)$$

where *h*, *k*, *l* are Miller indices and *x*, *y*, *z* are the coordinates of the atoms. This equation also can be expressed as:

$$F_{hkl} = |F_{hkl}|e^{-i\varphi} \quad (2.11)$$

where φ is the phase. The intensity of a reflection depends on the squared magnitude of the structure factor (Stout & Jensen, 1989), which mathematically can be expressed as:

$$I_{hkl} \propto |F_{hkl}|^2 \quad (2.12)$$

2.6.2 Structure Solution and Phase Problem

According to equation 2.12, the information of phase is lost during diffraction, because only the intensity (and with this the modulus of the structure factor) can be measured experimentally. As a result, reconstructing the crystal structure directly from the observed diffraction data becomes impossible without prior knowledge of the phase information. This fundamental challenge in crystallography is known as the phase problem.

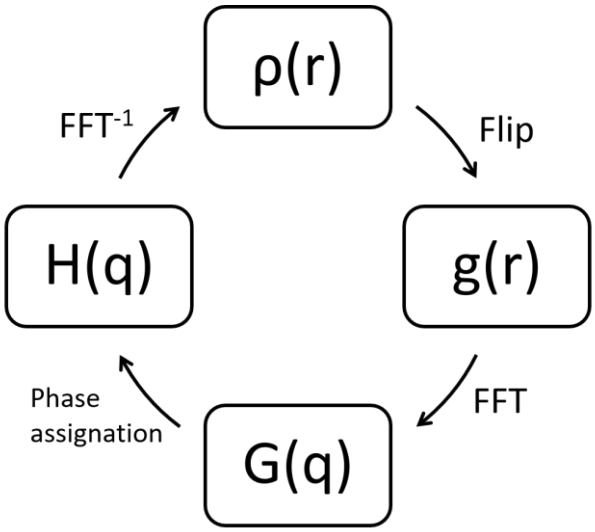

Figure 8: A chart demonstrating the principle of charge flipping (figure after Palatinus, 2013)

To solve the phase problem, there are different methods employed such as direct methods (see e.g. Schenk, 1984), the Patterson method (see e.g. Rossmann & Arnold, 2006), the charge flipping algorithm (see e.g. Palatinus, 2013) etc. In this thesis, the charge flipping method has been utilized using Superflip (Sheldrick et. al., 2012), which is distributed with the *Jana 2006* software (Petříček et. al., 2014). This method was employed to determine an initial structural model for subsequent refinement. The algorithm of charge flipping (figure 8) is:

1. Phases are randomly assigned to all observed reflections.
2. The electron density using these random phases is obtained using the inverse Fourier transformation.
3. Negative electron density values are replaced with their positive counterparts, generating a modified electron density $\rho_m(x,y,z)$.
4. Temporary structure factors G_m are calculated from $\rho_m(x,y,z)$.
5. The experimental amplitudes are combined with Gm to calculate new structure factor F_{n+1}.
6. Step 2 to 5 are repeated until the procedure converges. (Palatinus & Chapuis, 2007)

2.6.3 Structure Refinement and Least Squares Method

Once a satisfactory initial structural model is obtained, one can start with the structure refinement. In this step, structural parameters such as atomic positions and atomic displacement

(ADP) parameters[1] are refined by least squares method (Stout & Jensen, 1989). The least squares method is a mathematical technique which minimizes the differences between observed and calculated structure factors by changing structural parameters (Miller, 2006). Since X-ray diffraction occurs primarily via electron clouds, heavier atoms become scatters stronger than lighter ones. The refinement of structural parameters thus goes subsequently from the heaviest to the lightest atom.

The criterion for convergence is the overall agreement factors called *R*, which can be expressed as:

$$R = \frac{\sum|F_{obs} - F_{calc}|}{\sum|F_{obs}|} \; and \; R(F^2) = \frac{\sum|F_{obs}^2 - F_{calc}^2|}{\sum|F_{obs}^2|}$$

where F_{obs} and F_{calc} refer to the observed and calculated structure factor, respectively.

[1]ADP parameters are parameters which describes how much the atom oscillates around the average position.

3 Experimental methods

In this chapter, various experimental methodology and the sample description will be introduced. The magnetic characteristic of the sample is determined by SQUID (MPMS) and Dynacool (VSM) measurements and the subsequent corrections applied to the data. The crystallographic characteristics are determined by single crystal data measured with the *SuperNova* and ESRF synchrotron data which are processed by *CrysAlis^{Pro}* (v171.42.80A; Rigaku Oxford Diffraction, 2023), *Jana 2006* (Petříček et. al., 2014) and/or *Jana 2020* (Petříček et. al., 2023).

3.1 Sample description

In this section we provide a brief overview of the samples investigated in this thesis, including their synthesis timelines and the methodology adopted for sample preparation. Three sets of samples were synthesized at different time frames and analysed to study their spin-crossover (SCO) behaviour under various experimental conditions.

Sample Set 1: SC-2021

- Synthesis: 2021 (Hüppe, 2023)
- Description: Single-crystal samples
- Experimental Findings:
    - Initial magnetization measurements indicated the presence of spin-crossover (SCO).
    - However, repeated magnetization measurements approximately one month later showed no observable SCO.
    - To investigate further, single-crystal X-ray diffraction was performed at the European Synchrotron Radiation Facility (ESRF) with fine temperature steps, but no SCO transition was detected (see section 4.2.3.2).

Sample Set 2: SC-2023

- Synthesis: 2023 (Hüppe, 2023)
- Description: Single-crystal samples
- Experimental Findings:
    - Magnetization measurements revealed SCO behaviour.
    - In-house single crystal X-ray diffraction measurements performed at RT and 97 K showed a clear SCO transition.

Sample Set 3: SC/P-2025

- Synthesis: 2025 (Hüppe, 2023)
- Description:

- SC-2025(Single Crystals)
- P-2025 (Powder Samples)

- Experimental Findings:
  - Magnetization measurements confirmed that only the single-crystals undergo SCO, while the powder (P-2025) shows no SCO (see section 4.1).
  - Structural investigations were performed on the SC-2025 samples using the in-house diffractometer (see section 3.4.1)

To further clarify the designation of different samples mentioned in the thesis, the nomenclature of the samples with their time frames and their magnetic behaviour is listed in table 2.

Table 2: Nomenclature of samples

Sample name	Year of synthesis	Sample form	Whether has SCO?
SC-2021	2021	Single crystals	YES, after one month, NO
SC-2023	2023	Single crystals	YES
SC-2025	2025	Single crystal	YES
P-2025	2025	Powder	NO

3.2 Synthesis Methodology

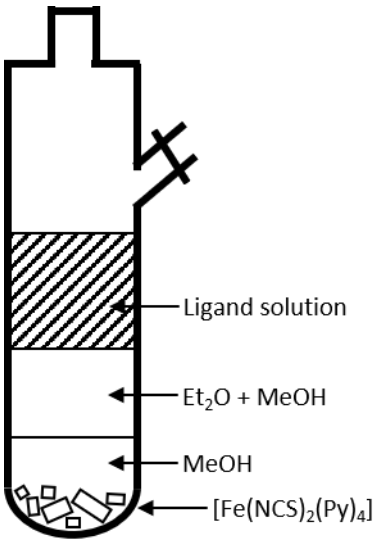

Figure 9: Synthesis process of the compound

The synthesis of the single crystals involves a three-layer solvent system designed to enable slow diffusion and controlled crystal growth (Hüppe, 2023):

1. Ligand Solution Preparation:

First, the solid ligand (tris(quinoline-8-yl)amine) is dissolved in a solvent which consists of diethyl ether (Et_2O) and methanol (MeOH) with a ratio of 1:1.

2. Salt Suspension:

MeOH is then used to suspend the salt $Fe(NCS)_2(Py)_4$, which is insoluble in MeOH. This suspension forms the bottom layer.

3. Layer Formation:

The second layer is added on the top of the thiocyanate salt suspension. This layer consists of 1:1 mixture of MeOH and Et_2O. Then, the previously prepared ligand solution is layered on the top as the third layer.

An illustration of the three layers is shown in figure 9. In this configuration, the ligand solution and the thiocyanate salt interact slowly, therefore creating a good environment for the growth of single crystals. However, if the tube is shaken immediately after the three layers are added together, rapid mixing occurs, leading to the formation of powder samples instead of single crystals. More detailed information can be found in Hüppe, 2023.

3.3 Determination of Magnetic properties

3.3.1 SQUID (MPMS)

3.3.1.1 Experimental Equipment and Mechanism

The effect of the spin transition on the magnetic susceptibility of the SCO material is investigated by utilizing the Magnetic Property Measurement System MPMS which is a Superconducting Quantum Interference Device (SQUID). SQUID is a sensitive magnetometer (10^{-8} emu) and is usually utilized for measuring the magnetic moments of small samples. The applied external field is produced by the superconducting magnets in the SQUID and reaches from -7 T to 7 T. In addition to the applied field, the instrument is also capable of varying the temperature from 1.9 - 400 K, allowing the control of step size and scan rate (dT/dt).

As shown in figure 10, the sample is placed in the middle of a plastic straw. Then, it moves up and down through the pick-up coils. During the experiment, the magnets apply an external field to the sample. As the sample moves, any changes in its magnetic moment induce signals in the pick-up coil. These signals are subsequently transferred to the rf- (radio-frequency) SQUID ring, which converts the magnetic moment variations into voltage changes that are easier to measure accurately.

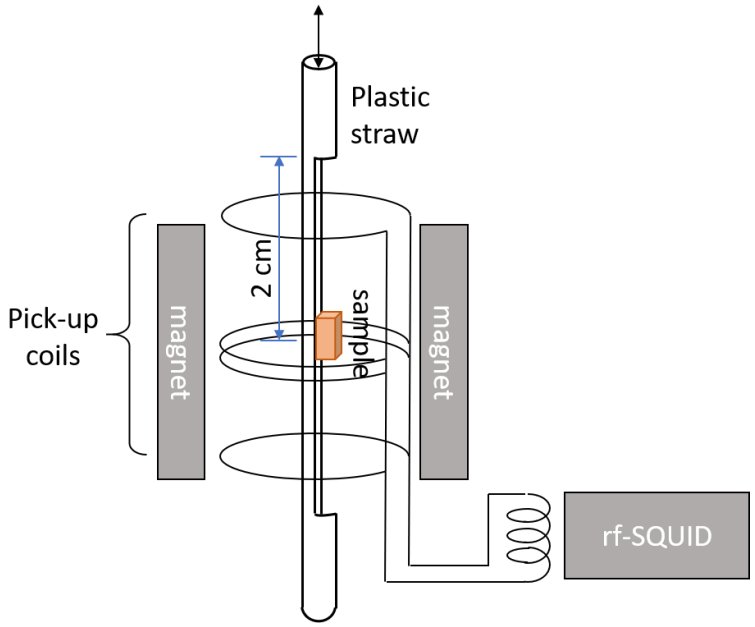

Figure 10: Schematic instrument setup of a MPMS XL system using a rf-SQUID ring

There are two options for the sample transport: direct current (DC) and reciprocating sample option (RSO). The DC technique is a stepped scan method which starts from the bottom and then sequentially moves the sample upwards to the predefined scan length through the superconducting pickup coils. Once the scan is completed, the sample returns to its starting position. The RSO scan, however, starts from the centre of the scan length. Then it scans firstly downward, then upward, and finally back to the centre. Normally, DC scan is more sensitive than RSO scan. However, the measurement time is relatively longer. Therefore, DC scan is more beneficial when a higher moment sensitivity is required for a measurement.

3.3.1.2 Experimental Procedure

The plastic straw, on which the SCO crystals are to be mounted, is first flattened by 2 cm on either side of its centre. Then the crystals of SC-2025 (sample description see section 3.1) are placed at the centre of the straw and their position is fixed using tapes. The straw holding the crystals is then coupled to the sample holder rod of the MPMS and the entire assembly is lowered down in the MPMS chamber (Fagaly, 2006).

Figure 11: MPMS XL system

Before starting the measurement, the sample needs to be centred within the pick-up coils, which is done by performing a DC or RSO scan in the presence of an applied field. Once the sample is properly centred, the measurement protocol (detailed below) can be initiated.

The experiments performed for this thesis consist of three processes:

(i) Zero Field Cooling (ZFC): The sample is first cooled in the absence of an external magnetic field, and then it is warmed up under an applied magnetic field during which the magnetization is recorded.

(ii) Field-Cooled Cooling (FCC): This process is carried out by cooling the sample under an applied external magnetic field, while simultaneously measuring its magnetization.

(iii) Field-Cooled Warming (FCW): Similar to FCC, the sample also is cooled down in an applied magnetic field. However, in this process, the magnetization is measured while the system is warmed up in the presence of field.

The measurements according to the protocols listed above were performed in a temperature range of 20K ⩽ T ⩽ 300K, using different scan rates, namely 10 K/min, 8 K/min, 5 K/min, 2 K/min, 1 K/min, and 0.8 K/min, under an applied external magnetic field of 500 Oe.

3.3.2 Dynacool (VSM)

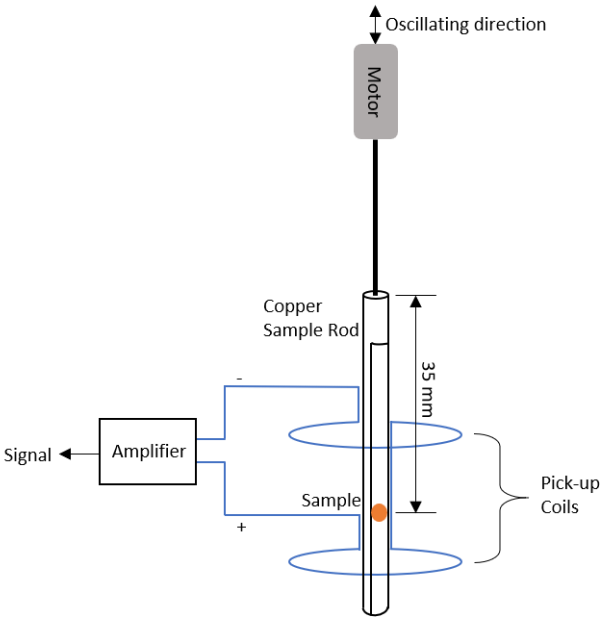

Figure 12: Illustration of Dynacool with VSM option

The Quantum Design Dynacool-PPMS (Physical Property Measurement System) is a sensitive (accuracy of about 10^{-6} emu) equipment that can measure different physical properties in a temperature range from 1.4 K to 400 K under an applied magnetic field in the range of ± 9 T.

In this machine, the magnetic measurement is performed by a VSM option (Vibrating Sample Magnetometer) whose setup is illustrated by figure 12. In the VSM option, the sample oscillates with a 2 mm amplitude at a frequency of 40 Hz. According to Faraday's law, this oscillation within a uniform magnetic field induces an AC voltage in the pick-up coils due to slight variations in the sample's magnetic moment. Then, the voltage signal is amplified, and converted back to the magnetic moment according to the following formula:

$$V_{coil} = 2\pi f C m A sin(2\pi f t)$$

where *f* is the frequency with which the sample oscillates; *C* is the coupling constant; *A* is the amplitude of sinusoidal oscillation; and m is the magnetic moment of the sample.

The measurements in this machine were carried out on P-2025. To load the sample, it is firstly filled in a plastic capillary and then secured on to a copper rod (see figure 12). Then, similar to the measurements in the SQUID, this entire assembly is lowered down in the Dynacool and a centring procedure is preformed (Quantum Design, 2019).

Following this the magnetization of the sample is measured using the FCC and FCW protocol, in the same applied field, scan rates and temperature range, as in the case of measurements with SQUID.

Figure 13: Photo of Dynacool

3.4 Single-Crystal Diffraction

3.4.1 SuperNova

The *SuperNova* single-crystal diffractometer (Rigaku Oxford Diffraction, Tokyo, Japan) is a four-circle Kappa geometry diffractometer (figure 14). It is equipped with two switchable X-ray tube allowing utilization of both Cu (Kα = 1.5418 Å) and Mo (Kα = 0.7093 Å) as target material. The temperature of the measurement environment can be controlled by a nitrogen gas flow with cooling capabilities down to 90 K, and heating up to 400 K. The schematic diagram of the instrument is shown in figure 15.

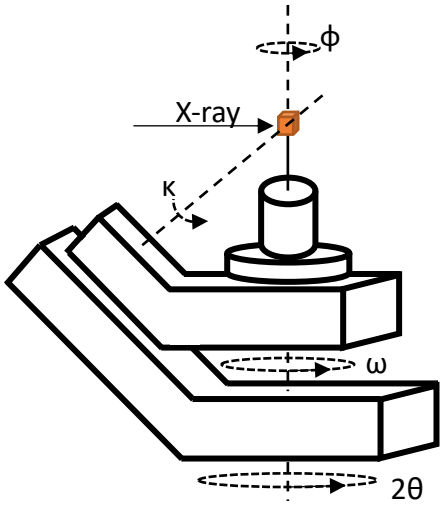

Figure 14: Schematic of the Kappa geometry diffractometer

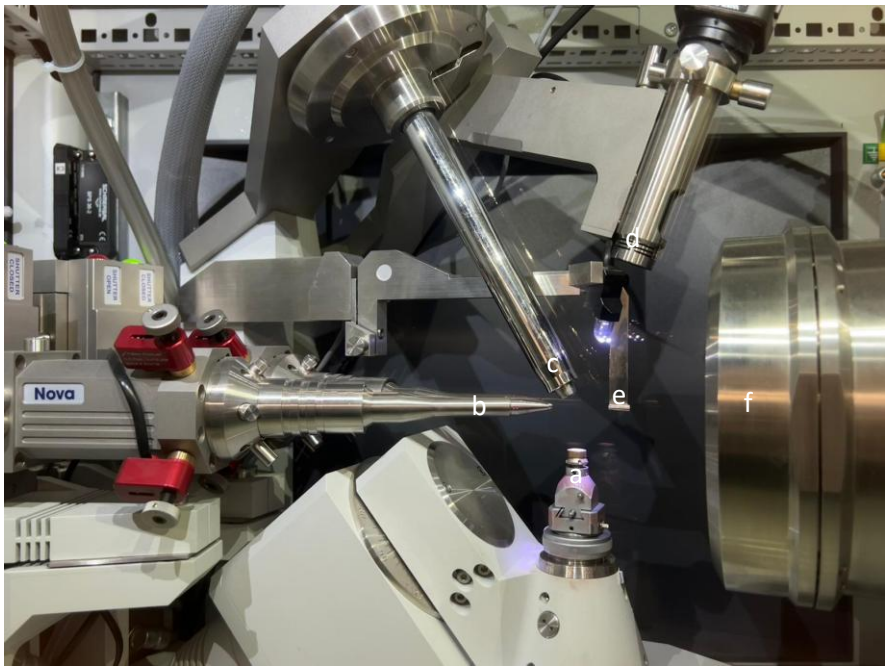

Figure 15: A photo of the *SuperNova* single-crystal diffractometer:
a) goniometer head; b) incident X-ray beam; c) N_2 flow cryojet; d) high-resolution camera; e) beamstop; f) beryllium window and 2D-detector.

An idiomorph crystal was chosen from SC-2025 having a size of 50-100 μm, with flat and smooth faces and well-formed crystalline shape. The selected crystal was then glued on the tip of a glass fiber by a two-components commercial glue. The glass fiber was fixed on a brass pin. The diameter of the glass fiber was approximately the same as the chosen crystal. Then, the crystal was mounted on the head of the goniometer and centred using a high-resolution camera. Successful centring was achieved when the single crystal remained illuminated by the incident beam at all orientations regardless of how the crystal was rotated around different axes.

After that, a pre-experiment at room temperature was performed to check for any defects or mosaicity in the crystal. The quick experiment had an exposure time of 40 sec. If the crystal diffracted well, then the crystal was preserved for a full measurement. It is crucial to note that calibration was performed prior to the full experiment. Calibration aimed to obtain an accurate orientation matrix enabling precise indexing by obtaining detector parameters. This process required a standard material with known lattice parameters. In this study, ruby was used as a reference material. The ruby lattice parameters are $a = b = 4.760(3)$ Å, $c = 12.9957(9)$ Å (Wong-Ng et. al., 2001).

After calibrating, a full experiment of the fresh crystal was carried out, keeping the exposure time as 40 sec with the step width of 1°. The resolution and the data redundancy were set to 0.8° and 8, respectively. On the basis of these parameters, the strategy for the collection of the data was determined using the algorithms included in the diffractometer software. To avoid the strong fluorescence of Fe atoms, Mo radiation was used in the single crystal diffraction experiment.

Due to the unexpected cracking of the single crystals during the cooling process, single crystal diffraction experiments on *SuperNova* were performed in two strategies:

(i) Warming Cycle:

The diffraction data was first recorded at 300 K to identify the structure in ambient conditions. Following this the crystal was cooled down to 95 K, after this it was attempted to record the data on warming to 300 K. Nevertheless, the crystal was found to break after the experiment at 95 K. Therefore, a second strategy was chosen to obtain more data points without breaking the crystal.

(ii) Cooling Cycle:

In the second strategy we planned to record the data while cooling through the temperature points 300 K, 200 K, 170 K, 140 K, 110 K and 95 K. After recording at 95 K, the crystal was supposed to be warmed up to 300 K again to identify the difference in crystal structure after cooling. This time, the crystal broke after the experiment at 110 K.

3.4.2 ESRF (synchrotron) Data

The ESRF is the European Synchrotron Radiation Facility. The experiment was performed at the Swiss Norwegian Beamlines (van Beek et. al., 2011) at experimental hutch BM01 with a wavelength of 0.655(5) Å. The resolution and the beam size were set to be 0.651° and 300×270 μm, respectively. A single crystal of Alum ($KAl(SO_4)_2$) was used for the calibration of the instrument. The temperature was initially ramped up to 350 K at a rate of 360 K/h, without collecting any data. After this, the sample (here we used aged sample 2020) was cooled down

to 90 K with the same scan rate, and the data was collected in steps of 10 K from 350 K to 170 K and in steps of 2 K from 168 K to 90 K. Following this, in the heating cycle from 90 K to 195 K the data was collected in steps of 5 K and in steps of 20 K from 200 K to 340 K. Unlike the experiments performed on *SuperNova*, the crystal did not crack during the measurement in ESRF.

3.5 Data processing

3.5.1 Magnetic data processing

3.5.1.1 Data correction

The magnetic moment measured on SQUID or Dynacool includes contribution not only from the compound, but also the background signals from the sample holder. The measured magnetic moment is corrected based on the Cure-Weiss law. The correction is performed in the following way:

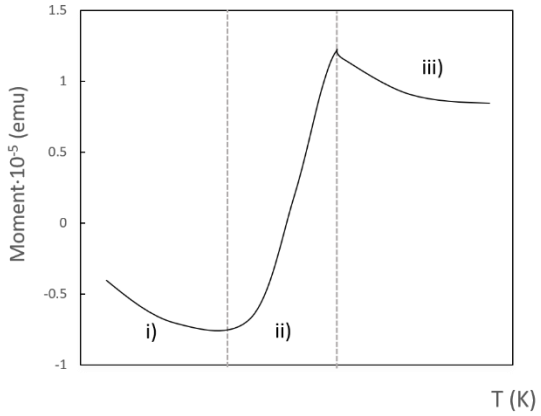

Figure 16: An illustration of the subdivided regions in magnetic data correction: i): LS region; ii): SCO region; iii): HS region.

1. Each curve of measured magnetic moment in the whole temperature range is subdivided into three regions: i) the LS region, ii) the SCO region in which the SCO is occurring, and iii) the HS region (see figure 16).
2. The magnetic moment in region i) is fitted by a function: $M' = \alpha + \frac{\beta_1}{T}$, where α refers to the diamagnetic contribution of background signals in the LS and β_1 is the paramagnetic contribution of background.
3. The magnetic moment in region iii) is fitted by a function: $M'' = \alpha + \frac{\beta_2}{T}$, where α is set to be the same as in the LS and HS state and β_2 refers to the paramagnetic contribution of background in HS state.
4. Then, the whole magnetic moment data is corrected by

$$M_{corr} = M - (\alpha + \frac{\beta_2}{T}) \quad (3.1)$$

as the diamagnetic contribution of background signals dominates at the LS state, while in the HS state, paramagnetic contributions of background signals are much more dominant than in the LS state.

3.5.1.2 Calculation

After the correction is completed, several parameters are calculated to visualize the SCO phenomenon more clearly, using the following formulas:

$$\chi_M \cdot T(cm^3 \cdot K \cdot mol^{-1}) = \frac{M_S(emu) \cdot T(K) \cdot M(\frac{g}{mol})}{H(Oe) \cdot m(g)} \quad (3.2)$$

where χ_M is the molar susceptibility; M_s is the magnetic moment of the sample; T is the temperature, M is the molecular weight; H is external field strength; and m is sample mass. The high spin fraction γ_{HS} is calculated according to:

$$\gamma_{HS} = \frac{(\chi_M \cdot T)_{min} - \chi_M \cdot T(T)}{(\chi_M \cdot T)_{min} - (\chi_M \cdot T)_{max}} \quad (3.3)$$

where $(\chi_M \cdot T)_{min}$ and $(\chi_M \cdot T)_{max}$ are the minimum and the maximum value of $\chi_M \cdot T$ from each cooling or warming process, respectively; and $\chi_M \cdot T(T)$ is the $\chi_M \cdot T$ value at any temperature T.

$T_{1/2}$, represents the temperature at which half of the sample molecules underwent the SCO transition. The hysteresis is calculated according to:

$$Hysteresis = T_{1/2}^{\uparrow} - T_{1/2}^{\downarrow} \quad (3.4)$$

where $T_{1/2}^{\uparrow}$ and $T_{1/2}^{\downarrow}$ are the $T_{1/2}$ during the warming process and the cooling processes, respectively.

3.5.2 Data reduction for single-crystal diffraction

3.5.2.1 Data reduction

Prior to structure determination, various treatments, including corrections and the background subtraction have to be applied to the raw data (Milburn, 1973). In this study, the raw data were processed using *CrysAlis*^{Pro} (v171.42.80A; Rigaku Oxford Diffraction, 2023).

In *CrysAlis*^{Pro} peaks are identified by comparing the intensity of each pixel with its local background. The software detects peaks above a certain intensity threshold in the diffraction frames and creates a peak list.

Each reflection is assigned to its corresponding reciprocal vector (*h*, *k*, *l*) using the built-in algorithms for indexing the diffraction pattern and the orientation matrix is determined. The orientation matrix converts the Cartesian coordinates (x, y, and z) to the Miller indices of the reciprocal vector. Their connection can be expressed as:

$$\begin{pmatrix} x \\ y \\ z \end{pmatrix} = UB \begin{pmatrix} h \\ k \\ l \end{pmatrix} \quad (3.5)$$

where *U* and *B* are two matrices. *U* describes the orientation of crystal axes with respect to the laboratory reference system, while *B* represents information about the unit cell parameters.

During peak indexing, the orientation matrix serves as a basis to predict the position of Bragg reflections and results in the lattice parameters. A least-square refinement of the *UB* matrix is performed to minimize the difference between the calculated peak positions and the observed ones.

After this step the lattice parameters are refined. The detector parameters are determined from the instrument calibration using a reference material (see section 3.4.1). During the integration, all diffraction intensities which are not indexed by the program and do not fall onto lattice points predicted by the *UB* matrix are not taken into account.

3.5.2.2 Corrections to the Integrated Intensities

The measured intensity in an X-ray diffraction experiment is proportional to the square of the structure factor ($|F_{hkl}|^2$). Accounting for various experimental factors, the corrected intensity can be expressed as:

$$I_{hkl} = S \cdot L \cdot P \cdot Abs \cdot Ext \cdot |F_{hkl}|^2 \tag{3.6}$$

where *S* stands for scaling factor, *L* for Lorentz factor, *P* for polarization factor, *Abs* for absorption correction, and *Ext* for extinction correction.

The scaling factor is a refinable constant, which depends on the instrument and experimental setup. The Lorentz factor (*L*) takes into account the fact that different reflections spend different amounts of time in the diffraction conditions depending on their scattering angle (Stout & Jensen, 1989).

When the X-ray passes through a crystal, a part of the intensity is absorbed in accordance with the Lambert-Beer law $I = I_0 e^{-\mu d}$, where μ (cm^{-1}) is the linear absorption coefficient depending on different materials; *d* (cm) is the thickness of the crystal; I_0 is the incident intensity and *I* is the transmitted intensity after absorption by the crystal.

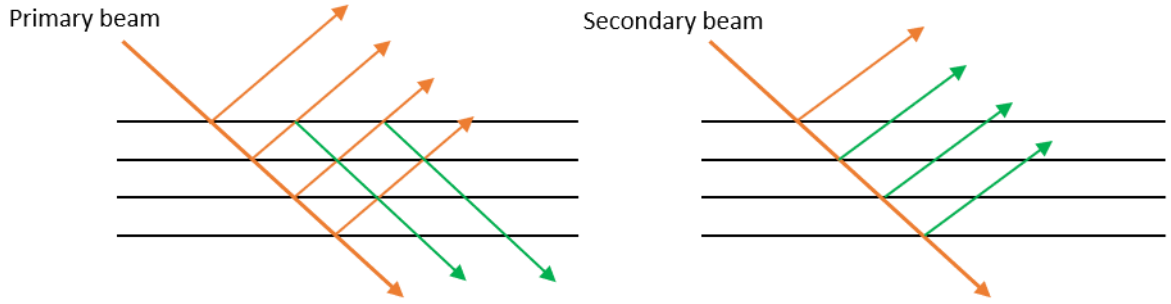

a) b)

Figure 17: Schematic representation of extinction in crystal lattice planes: a) primary extinction; b) secondary extinction; orange arrows represent beams in phase; and green arrows represent beams out of the phase.

For the Mo target radiation, the linear absorption coefficient of metalorganic crystals is usually much smaller compared to data collected with Cu Kα radiation (Stout & Jensen, 1989). Therefore, the absorption correction does not have a huge effect. By comparing groups of observed *F* and calculated *F*, an absorption correction can be generated (Stout & Jensen, 1989). When the crystal faces are well defined and can be accurately indexed, a numerical method can be used for absorption correction (analytical or Gaussian quadrature methods).

In this study, Gaussian quadrature methods is used. The Gaussian quadrature methods is based on the following formula:

$$\int_a^b W(x)f(x)dx = \sum_{i=1}^{n} w_i f(x_i) \quad (3.8)$$

where *W(x)* is the weight function, w_i is the weight of each node and x_i are nodes (Branders & Piessens, 1971).

All the corrections mentioned are performed in *CrysAlis^{Pro}*. After the corrections, *CrysAlis^{Pro}* produces the cif, cif_od and hkl files for further data treatment in *Jana 2006* software. The extinction corrections are performed in *Jana 2006* (Petříček et. al., 2014). Extinction occurs in high quality crystals, where $F_{obs} < F_{calc}$ at low scattering angles.

According to Darwin's classification, there are two types of extinction: primary and secondary extinction (Milburn, 1973). Primary extinction exists when the incident X-ray beam undergoes a destructive interference with the beams that are reflected from the lattice planes (green arrows in figure 17a). Secondary extinction occurs when the diffracted beam of the primary beam (the thin orange arrow in figure 17b) is further weakened by subsequent diffraction at deeper crystal planes (green arrows in figure 17b).

3.5.3 Structure Solution and Structure Refinement

Jana 2006 software suggests the symmetry options based on the fact that symmetry equivalent lattice planes possess the same intensity after extinction correction. The decision on space group is based on the analysis of systematic absences which is performed in *Jana 2006*. Once the space group is determined, the program merges all the intensities at symmetry equivalent position with an average I_{hkl} with a standard deviation (σ). SuperFlip which is implemented in *Jana 2006* is then used to find a starting structure model (see section 2.6.2). Afterward, the atomic coordinates and the anisotropic ADP parameters are refined sequentially from heavy atoms (iron), and subsequently from the lighter atoms (nitrogen, carbon, etc.). Hydrogen atoms are added using a riding model[2] with a C-H bond distance of 0.93 Å.

Finally, the Fourier difference map (F_{obs} - F_{calc}) is calculated to find the strongly disordered solvent atoms. After the positions of solvent atoms are revealed by Fourier difference map, reference C-C and C-O bond length can be used to identify the type and shape of solvent molecules. After a full refinement of the structure, the lattice parameters, bond length and bond angles are available. Therefore, the octahedral distortion parameter Σ can also be calculated by the following equation:

$$\Sigma = \sum_{i=1}^{12} |90 - \alpha_i| \quad (3.8)$$

where α is the N-Fe-N angles (Phonsri et. al., 2017).

For the sequential refinement of ESRF synchrotron data, the principles and procedure of data processing is exactly the same as mentioned before (except the polarisation correction (van Beek et. al., 2011)). The data processing is performed in *Jana 2020* (Petříček et. al., 2023) in a sequential way. The structure at 90 K is manually solved to give the program a starting model. After inputting all the reduced data from *CrysAlis^{Pro}* for each temperature, *Jana 2020* follows the structural refinement of the starting model and automatically performs the same refinement

[2]In the riding model, hydrogen atoms are located next to the heavy atoms which are directly bonded to them with a fixed bond length and ADP parameters. Their ADP parameters are deduced from the ones of the heavy atoms next to them.

for the data at all temperatures. As a starting model for each next higher temperatures the refined model from the temperature point just below is used. Results as a function of temperature (e.g. lattice parameter, bond lengths and angles) can be visualized at the end of the sequential refinement.

4 Results and Discussion

In this section, the results of magnetic and crystallographic investigations on the [Fe(NQu$_3$)(NCS)$_2$·0.5 Et$_2$O] compound will be presented and discussed. The correlations between the magnetic behaviour, crystal structure, and some specific properties of the compound are also investigated. In this thesis, magnetic measurements are carried out on the newest batch of synthesized material (SC-2025 and P-2025). For the single crystal diffraction, crystals from three different batches synthesized at different time are used (SC-2025, SC-2023, and SC-2021) (nomenclature see section 3.1).

4.1 Magnetic Characteristic

4.1.1 Magnetic Characteristics of SC-2025

The product of the molar magnetic susceptibility with temperature, χ_M T (of SC-2025), recorded as a function of temperature with a scan rate of 2 K/min, is shown in figure 18. The data has been corrected for diamagnetic and paramagnetic contributions, as described in section 3.5.1.1.

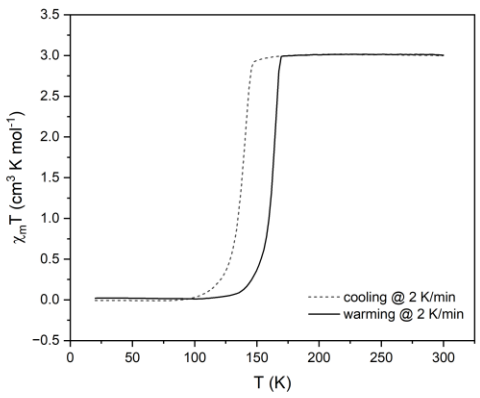

Figure 18: Plot of χ_M·T at a scan rate of 2 K/min

At room temperature, χ_M T has a value of 3 cm^3 K mol^{-1}, which is consistent with the expected value for a triplet HS state (S=2) (figure 18) (Chen et. al., 2019). Upon cooling, χ_M T exhibits a sharp decrease at 138 K ($T_{1/2}^{\downarrow}$), indicating a spin state transition of the Fe^{2+} ion from the HS to the low spin state (LS). Below 100 K, the magnetic response of the compound is almost zero, indicating the presence of a singlet LS state (S=0). In the heating cycle, χ_M T exhibits an abrupt increase at a temperature of 162.5 K ($T_{1/2}^{\uparrow}$), showing a transition from LS back to HS. The different transition temperatures during heating and cooling cycles indicate the presence of a thermal hysteresis with a net width of 24.5 K ($T_{1/2}^{\uparrow} - T_{1/2}^{\downarrow}$).

To investigate the scan rate dependence of the hysteresis width and $T_{1/2}$, magnetization measurements was further recorded with different scan rates (1, 2, 5, 8, and 10 K/min). According to γ_{HS}, calculated from χ_M T at each scan rate (method see section 3.5.1.2), shown in figure 19a, the $T_{1/2}$ associated with the cooling and the warming curves, shifts monotonically to lower temperatures with decreasing scan rates. However, this shift remains non-uniform with the cooling curves shifting more in temperature than the warming curves. Moreover, the thermal hysteresis width increases continuously with decreasing scan rate, which contrasts with some SCO compounds having no solvents such as Fe(n-Bu-im)$_3$tren (PF$_6$)$_2$ (Delgado et. al., 2018).

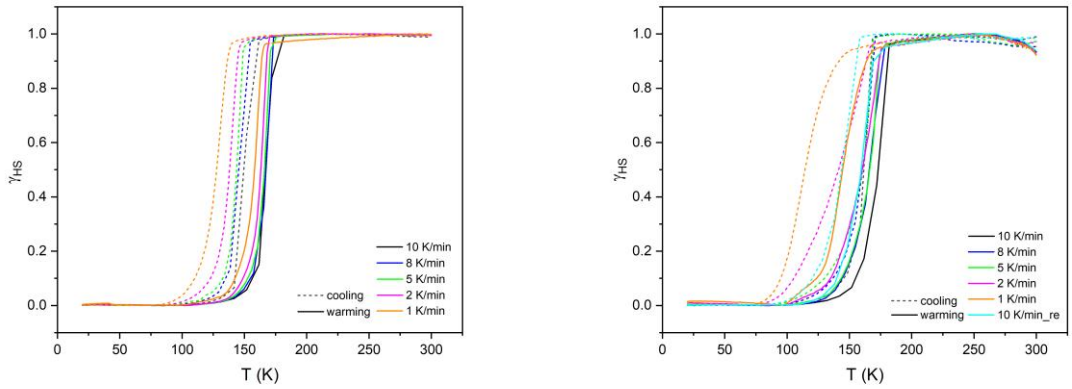

a) b)

Figure 19: Plots showing the temperature dependence of a) the high spin fraction (γ_{HS}) at different scan rates and b) the high spin fraction of repeated measurements at different scan rates (see sec 3.4.1.2 for details).

The $T_{1/2}$ and hysteresis width obtained with different scan rates are listed in table 3 and plotted in figure 20. The hysteresis at 1 K/min is more than twice the one at 10 K/min. With decreasing scan rate, $T_{1/2}$ decreases by 22.3 K during the cooling cycle which is much larger than the decrease observed during the warming cycle (6.4 K).

Table 3: $T_{1/2}$ and hysteresis at different scan rate

Scan Rate	1 K/min	2 K/min	5 K/min	8 K/min	10 K/min
$T_{1/2}^{\downarrow}$	127.7(3) K	138.0(5) K	144(1) K	145(2) K	150(3) K
$T_{1/2}^{\uparrow}$	157.6(3) K	162.5(5) K	164(1) K	165(2) K	164(3) K
Hysteresis	29.9(4) K	24(1) K	21(3) K	19(4) K	14(5) K

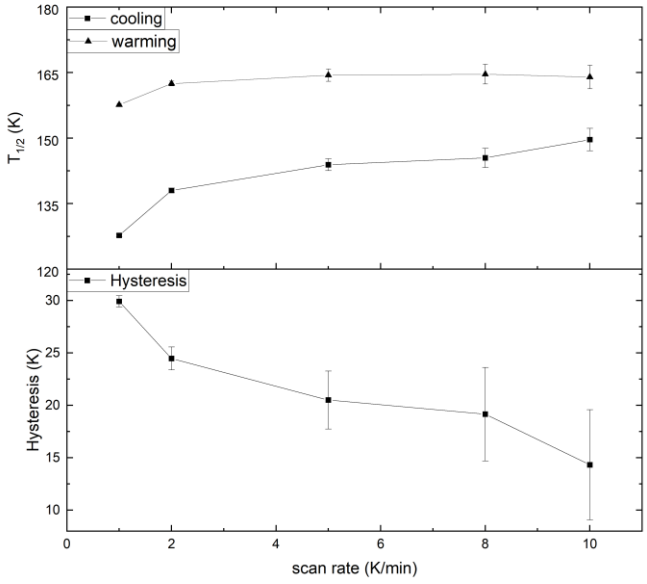

Figure 20: Scan rate dependence of the spin crossover behaviour derived from the magnetic susceptibility measurements: observed $T_{1/2}$ values on cooling and warming cycles (top) and thermal hysteresis width (bottom).

Literature on scan rate dependence of spin-crossover compounds is scarce, yet we still try to briefly discuss our results in comparison to previous studies. According to the examples discussed in the literature, SCO compounds which undergo a first order phase transition, can exhibit a (i) constant thermal hysteresis width which is independent of the scan rate (Shahed, 2024); (ii) a decreasing hysteresis with decreasing scan rate (Delgado et. al., 2018) or (iii) an increasing hysteresis with decreasing scan rate (Traiche et. al., 2017). In our case, we observe an increasing hysteresis width with decreasing scan rate. A similar case was observed in the compound $[Fe(n\text{-}Bu\text{-}im)_3(tren)](PF_6)_2$, where two distinct butyl conformations were observed leading to two distinct LS phases as a function of scan rate (Delgado et. al., 2018). From this, one might infer that in our case there are also kinetically driven distinct conformations of the solvent molecule, but in order to confirm this hypothesis, one would need to perform single crystal x-ray diffractions over multiple cooling and heating cycles.

It is worth mentioning that, after the SQUID measurement, the initial single crystals were fractured and could only be partially recovered in polycrystalline form. This indicates that, due to the first order nature of the SCO transition, multiple cycling across the transition temperature causes the crystal to break into several pieces, due to the large change in the lattice parameters (see section 4.2.1 and 4.2.2). Thus, the experiment was repeated on virgin samples with scan rate sequences of 10 K/min, 8 K/min, 5 K/min, 2 K/min, 1 K/min, and again 10 K/min. The purpose of repeating the measurement was to figure out whether the shift in the transition temperature with decreasing scan rate is related to the microstructure of the sample or to the scan rate variation.

The crystals were again found to be broken into several pieces in the repeated experiment. From figure 19b, we observe that the spin-phase fraction curves for the scan rate of 10 K/min, recorded at the beginning and the end of the measurement cycle, do not overlap with each other. Instead, the transition temperature of 10 K/min at the end of the experiment nearly matches with the observations at a scan rate of 2 K/min. This indicates that the breaking of the single crystal, and thus the particle size, influences the magnetization measurement. Thus, the increase of the hysteresis width with a slower scan rate is likely not only due to intrinsic kinetic effects of the spin transition but also to a physical degradation of the crystal.

The transition temperature of the scan rate 1 K/min has quite an offset when compared to the others and it shifts to even lower temperature when compared to the data measured in the previous experiment. This behaviour cannot be solely attributed to changes in particle size or sample shape. One possible explanation is that, at such a slow scan rate, the system had enough time to be trapped in a metastable structural state (might be solvent-related). This kinetic trapping might stabilize a different structural environment favouring the LS state at a lower temperature and leading to the observed shift.

Recent literature shows, that decrease in grain size can shift the hysteresis loop to lower temperatures and make its width smaller (Siddiqui et. al., 2021). While in our case, the grain size effect can well explain the shift of thermal hysteresis to lower temperatures, the increase in hysteresis width with decreasing scan rate is a contrasting result, which we believe could be linked to the solvent molecules present in our system.

The influence of the breaking of the crystal on the measurement results, might be an intrinsic effect related to the change in grain size of the sample, or, it might be related to the fact, that with the breaking of the crystal, the sample is smearing across the sample holder, causing a problem with the centring within the magnetometer.

4.1.2 Magnetic Characteristic of P-2025

Magnetization measurements, using Dynacool, on the P-2025 (powder samples) shows a pure paramagnetic signal at all scan rates (see figure 21). Furthermore, magnetic behaviour is almost identical in warming and cooling process, indicating the absence of a temperature induced SCO phenomenon within the investigated temperature range in the powder samples.

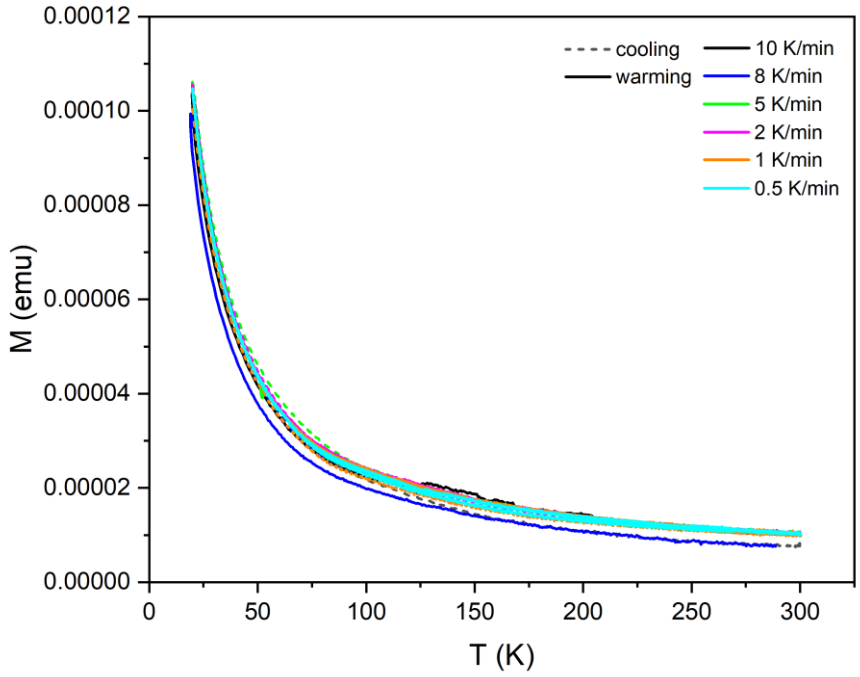

Figure 21: Magnetic moment of warming and cooling processes of P-2025 at different scan rates

We can assume two possible reasons to explain the contrasting results with respect to the macroscopic magnetization measurements on the two samples: (i) It is well known from the literature, that the presence of solvent molecules can be essential in enabling the thermal SCO transition (Fumanal et al., 2017). It is thus possible that the spin crossover (SCO) is not observed in the powder sample because, during precipitation from solution, it may have incorporated significantly less solvent—or even none at all—compared to the single crystals. (ii) the smaller grain size and higher surface-to-volume ratio of the powder could lead to faster solvent loss, possibly affecting the cooperative behaviour for the SCO. However, to our knowledge, complete suppression of SCO due solely to particle size has not been reported.

To further understand the difference of behaviour with respect to the SCO in both samples, further experiments such as temperature dependent single crystal and powder diffraction are needed.

4.2 Crystal Structure Characteristics

4.2.1 Crystal Structure of SC-2025 at Room Temperature

The space group of the compound $Fe(NQu_3)(NCS)_2 \cdot 0.5\ Et_2O$ at room temperature was found to be *C2/c* with the lattice parameters a = 9.9054(2) Å, b = 22.3828(7) Å, c = 25.8754(8) Å, β = 95.5840(20)°, and V = 5709.63(45) $Å^3$. There are in total 8 molecules in the unit cell, as illustrated in figure 22.

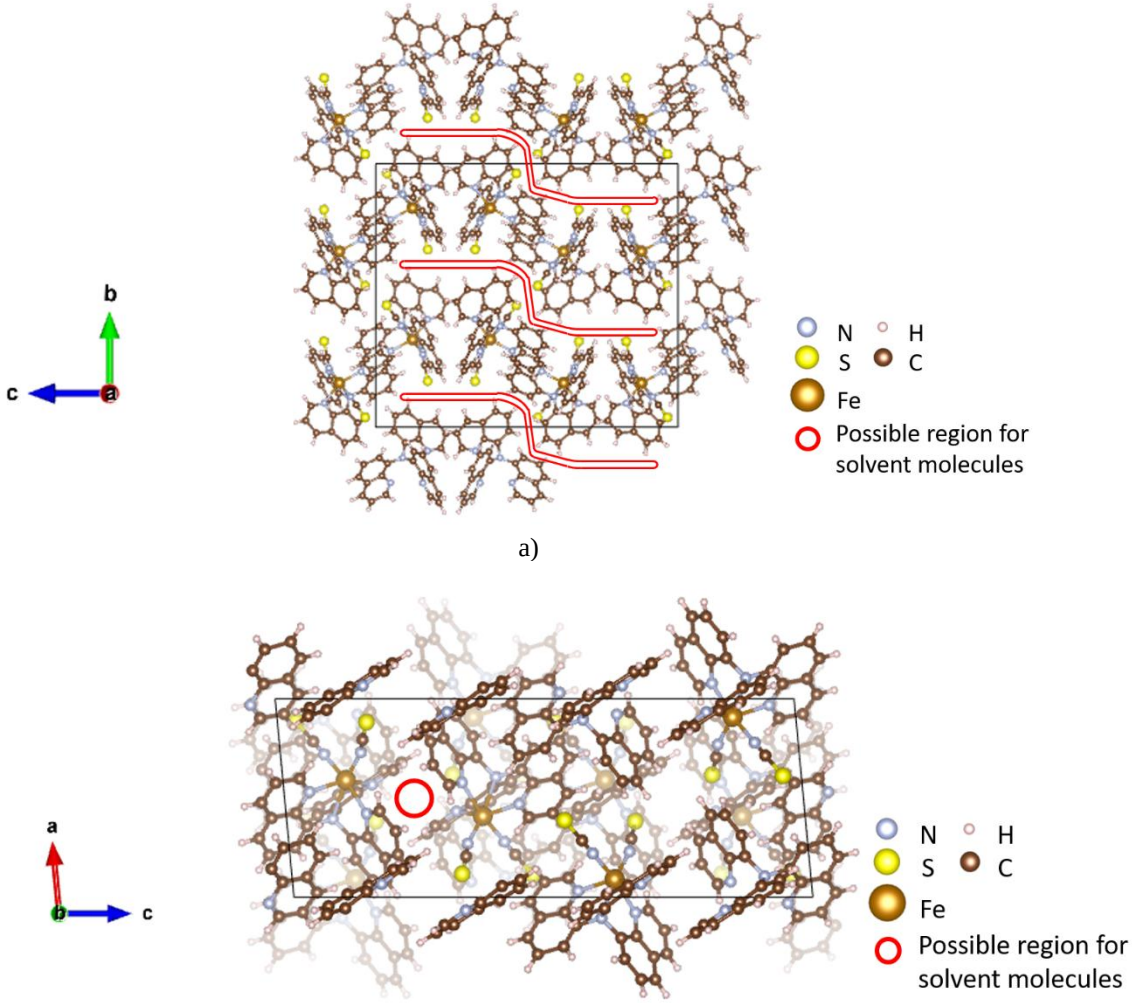

Figure 22: An illustration of $Fe(NQu_3)(NCS)_2 \cdot 0.5\ Et_2O$ crystal structure at room temperature: a) crystal structure along *a* axis; b) crystal structure along *b* axis. The red circle indicates the region where the solvent molecule most likely resides.

Taking into account only the Fe molecular complex without solvent molecules, the refinement of the crystal structure at room temperature yields an agreement of R(all) = 23.90, and weighted agreement factor wR(all) = 14.85, for all reflections with a goodness of fit (GOF) of 3.16.

At this stage of the refinement, an analysis of the Fourier difference map reveals several residual electron densities in the space between the molecular complexes near the two-fold axis. Incorporating these difference maxima in the refinement – in particular the most prominent one with a maximum positive peak height of 1.669 $e^-/Å^3$ in the difference Fourier synthesis map located on the special position (0.5,y,0.25) – leads to a significant improvement of the agreement factor (wR(all) from 14.85 to 13.24).

In the projection along *b* axis, the quinoline rings forms a "channel" which can accommodate solvent molecules (see the area circled with red lines in figure 22a and b). According to the Fourier difference map, most of the residual electron density is located in this region and we assume that the solvent molecules are incorporated here.

However, even when taking into account further maxima of the electron density difference, the determination of the precise chemical composition of the solvent molecules based solely on the bond lengths, bond angles and the electron density distribution remains challenging. This difficulty arises from two primary reasons. First, distinguishing between light elements (in particular with reduced occupation), such as C, O, and H is challenging using X-ray diffraction and second the observed bond lengths between the additional maxima are not easily assigned to the solvent molecules which were present during the synthesis. Consequently, an unambiguous assignment of the solvent molecules was not possible.

In contrast, the diffraction data of SC-2021 does not show the residual electron density at the special position observed from the diffraction data of SC-2025 and the electron density difference in the difference Fourier synthesis map drops to 0.432 $e^-/Å^3$. Instead, the maxima of electron density difference accumulate along the coordinate (0.5,0.45,z). This could be an evidence of the presence of solvent molecules in the SC-2023/SC2025 compounds investigated in *SuperNova* and their absence in the SC-2021 compounds investigated at ESRF. Summarizing, we can say that, although the type of solvent molecules is not unambiguously identified from the diffraction data, the presence (or absence) of solvent molecules and their potential positions in the lattices is confirmed.

4.2.2 Mosaicity

Mosaicity is an intrinsic property of each crystal and refers to the slight misalignment of several crystal domains, which broaden the reflection profiles. It is often associated with increased strain within the crystal. For our compounds, the single crystal x-ray diffraction data obtained using the in-house *SuperNova* diffractometer, show a significant increase in mosaicity in the diffraction frames collected at low temperatures (see figure 23). Due to this, we could not obtain reliable data integration for the low spin state of our compounds.

The increase in mosaicity on cooling is absent in the datasets of old crystals (SC-2021) which do not exhibit SCO. This further confirms that the SCO transition induces strain or micro-cracking, leading to a deterioration in the crystal quality and a significant reduction in the quality of the diffraction data.

The increase in mosaicity on cooling is also reported in other compounds (Lakhloufi et. al., 2018 & Guionneau et. al., 2012). For example, the compound $Fe(PM\text{-}PEA)_2(NCSe)_2$, which exhibits an abrupt SCO transition with a large hysteresis loop, undergoes an irreversible and abrupt increase in mosaicity during cooling (Lakhloufi et. al., 2018). In the case of the $Fe(PM\text{-}AzA)_2(NCS)_2$ compound, with a gradual thermal SCO transition, the maximum mosaicity appears around the SCO transition temperature (Lakhloufi et. al., 2018) and increases monotonically till 15 thermal cycles, after which a stable state is achieved (Guionneau et. al., 2012). The compound $Fe(PM\text{-}TeA)_2(NCS)_2 \cdot 0.5$ MeOH undergoes a gradual and incomplete SCO transition as a function of temperature (Lakhloufi et. al., 2018), and exhibits an irreversible increase in mosaicity across multiple thermal cycles through the SCO transition.

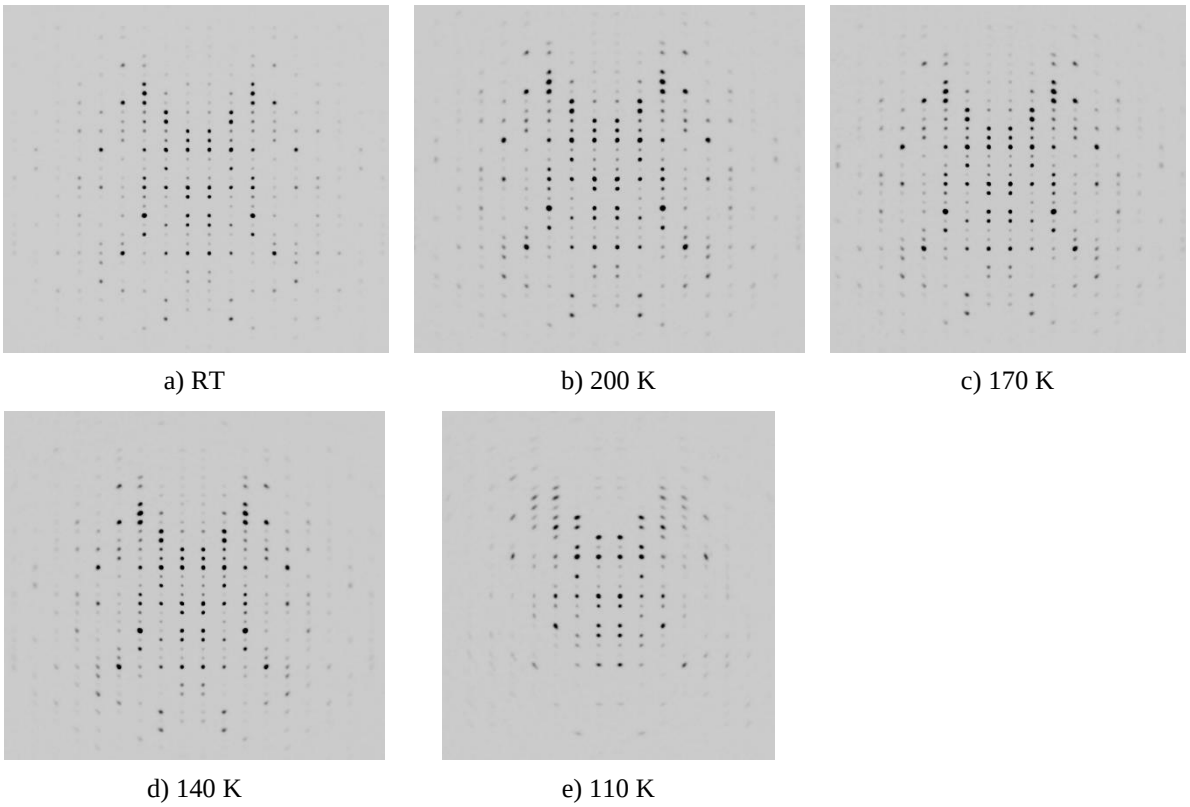

a) RT b) 200 K c) 170 K

d) 140 K e) 110 K

Figure 23: Reconstructed X-ray diffraction patterns of (1*kl*) plane at various temperatures: a) room temperature, b) 200 K, c) 170 K, d) 140 K, and e) 110 K, showing the increase in mosaicity on cooling

4.2.3 Temperature Dependence of Lattice Parameters

4.2.3.1 Lattice Parameters of SC-2025

A single and complete set of temperature dependent single crystal diffraction data could not be obtained from *SuperNova* for our samples (see section 3.4.1). Primarily, at low temperatures (below spin crossover $T_{1/2}$), the crystal was found to break in to multiple pieces, thereby disrupting the experimental run. Additionally, the increasing mosaicity on cooling made the acquisition of reliable intensities and data integration significantly more challenging.

Thus, for the diffraction data set at 95 K and 110 K, data integration was inconsistent and therefore structural refinement was unsuccessful. Consequently, only the lattice parameters were extracted directly from the initial data processing at 95 K and 110 K using *CrysAlis*^{Pro}. The lattice parameters, unit cell volume, agreement factors, etc. as a function of temperature are listed in table 4. Since three crystals were used in the measurement from 300 K to 95 K (see the notes in table 4), some small variation in the lattice parameters may occur. However, the general trend of lattice parameter variation remains. For reference, we also include a previously measured dataset, recorded at T = 97 K on the crystals from the batch SC-2023.

The compound was found to maintain the *C*2/*c* space group across all measured temperatures. The *a* and *c*-lattice parameters, along with β, were found to contract across the SCO, however the *b*-axis was found to exhibit a sharp increase below 140 K. This unusual trend of the *b*-axis is similar to the behaviour of the *c*-axis in $Fe(PM\text{-}PEA)_2(NCS)_2$ (Guionneau et. al., 1999) and

in monoclinic $Fe(PM\text{-}Bia)_2(NCS)_2$ (Marchivie et. al., 2003). All three compounds exhibit a first-order nature of spin-state transition, which is related to the negative thermal expansion.

Table 4: Lattice parameters, unit cell volumes, agreement factors, Fe-N bond lengths and distortion parameter (Σ) of $Fe(NQu_3)(NCS)_2 \cdot 0.5\ Et_2O$ measured on *SuperNova* single crystal diffractometer at different temperature points

Chemical Formula	$Fe(NQu_3)(NCS)_2 \cdot 0.5\ Et_2O$						
Space Group	*C*2/*c*						
T (K)	95	97	110	140	170	200	300
a (Å)	9.4321(5)	9.4726(8)	9.4715(7)	9.7811(3)	9.8001(3)	9.8123(2)	9.9054(2)
b (Å)	22.8902(13)	22.9550(20)	22.9670(20)	22.0500(9)	22.0840(7)	22.1184(7)	22.3828(7)
c (Å)	25.1726(17)	25.1749(14)	25.2180(20)	25.8161(9)	25.8500(7)	25.8672(7)	25.8754(8)
β (Å)	92.328(5)	92.2330(60)	92.3190(70)	96.2600(30)	96.1830(20)	96.1120(20)	95.5840(20)
V ($Å^3$)	5430.4(6)	5470(1)	5481.3(8)	5534.44(59)	5562.15(50)	5582.02(44)	5709.63(45)
R(all)	-	21.97	-	30.89	27.29	27.79	23.90
wR(all)	-	12.03	-	16.69	13.22	13.38	14.85
GOF(all)	-	1.65	-	2.84	2.32	2.36	3.16
$Fe\text{-}N_1$ (Å)	-	2.026(7)	-	2.331(8)	2.331(8)	2.332(8)	2.346(8)
$Fe\text{-}N_2$ (Å)	-	1.948(8)	-	2.075(10)	2.0750(15)	2.077(9)	2.060(11)
$Fe\text{-}N_3$ (Å)	-	1.924(8)	-	1.998(11)	2.074(9)	2.018(10)	2.042(11)
$Fe\text{-}N_4$ (Å)	-	1.947(7)	-	2.184(10)	2.182(9)	2.181(10)	2.206(10)
$Fe\text{-}N_5$ (Å)	-	1.939(8)	-	2.169(11)	2.161(11)	2.161(12)	2.186(11)
$Fe\text{-}N_6$ (Å)	-	1.931(8)	-	2.129(9)	2.116(9)	2.130(9)	2.158(10)
Σ (°)	-	42(1)	-	101(2)	99(1)	100(1)	100(1)

* Data at 97 K was recorded on the crystal from SC-2023 batch. Data at 95 K and data from 300 K to 110 K were recorded from two different crystals from SC-2025 batch.

* The correlation between $Fe\text{-}N_n$ bond (n = 1, 2, …, 6) and compound structure sees figure 26c.

It is worth noting that the mosaicity of the crystal starts to develop already at 170 K, and is further increased as the temperature decreases. The increase in the mosaicity leads to larger internal R value for the dataset measured at 140 K compared to other temperature points (see table 4). Further investigations, potentially involving much slower cooling down of the crystal over the SCO transition, might be a possible way to overcome these problems and achieve data of higher quality at these low temperatures.

The abrupt change in the lattice parameters, between 110 K and 140 K, correlates well with the SCO transition observed in the magnetization measurements (see section 4.1.1). We believe that the significant and sudden changes in the lattice parameters during the SCO transition induce crystal fracture, resulting in increased mosaicity. This observation is consistent with the behaviour of the crystals during SQUID experiments, where the crystal is also found to shatter in to several pieces over several cycles across SCO.

4.2.3.2 Lattice Parameters of SC-2021

A crystal of SC-2021 was measured with fine temperature steps at the Swiss Norwegian Beamlines at the ESRF. The data reduction was carried out using sequential data integration as implemented in *CrysAlis*^{Pro}. The structural data were refined using sequential refinement with the *Jana 2020* software (Petříček et. al., 2023) with solvent molecules excluded from the model. The results of these data along with the *SuperNova* datasets measured on SC-2025 are shown in figure 25.

Although these crystals no longer exhibit a SCO transition, it is still worth to investigate them as the different temperature dependent behaviour of lattice parameters from the ones obtained from SC-2023 and SC-2025 may reveal some features of SCO transition and the incorporation of solvents in these compounds.

The ESRF data of SC-2021, shows that the lattice parameters *a*, *b*, *c*, and the unit cell volume (V) decrease (see figure 25 and 24a) with decreasing temperature, while the β angle increases. Apart from the c lattice parameter and β angle, all the lattice parameters show a nearly linear correlation with temperature.

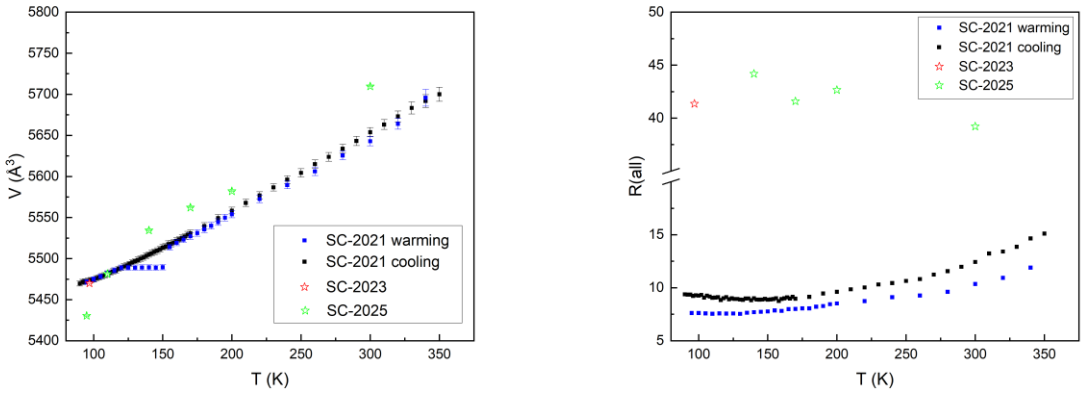

a) b)

Figure 24: Comparison of unit cell volumes (V) and agreement factor R(all) between SC-2021, SC-2023 and SC-2025: a) unit cell volumes; b) agreement factor.

The data collected during the cooling and the warming process appears to be identical albeit an anomalous increase in the lattice parameters between 150 -155 K during the warming cycle is observed. A close inspection of the diffraction frames and reconstruction images reveals no such anomalies in the raw data, suggesting that this jump could originate from a systematic error. A possible explanation would be that due to an error, the system failed to warm up the sample and that the sample temperature remained at 150 K longer than expected. Apart from this, no major differences are observed between the warming and cooling cycles, indicating reversible structural changes without significant hysteresis. This suggests that while the SCO transition is absent in these crystals and the structure remains stable with no major rearrangements upon cooling.

Also, due to the absence of the SCO transition, there is no substantial increase in the mosaicitiy of the crystals, which leads to better data quality at lower temperatures.

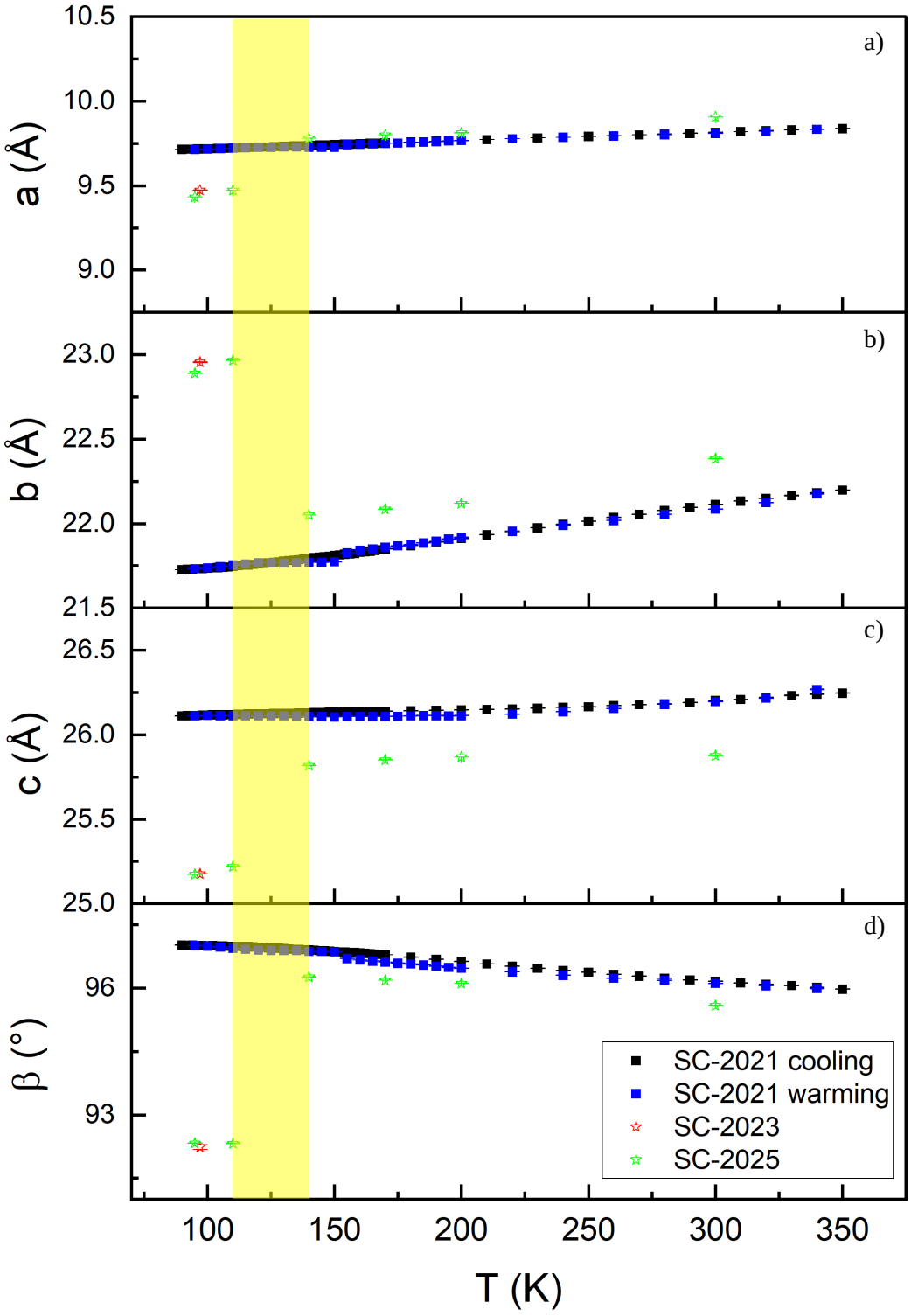

Figure 25: Comparison of lattice parameters between SC-2021, SC-2023 and SC-2025: a) lattice parameter *a*; b) lattice parameter *b*; c) lattice parameter *c*; d) monoclinic angle β. The highlighted area is the temperature range where the lattice parameters significantly changed in sample SC-2025.

4.2.4 Comparison between SCO and non-SCO Crystals

By comparing the crystals SC-2025, SC-2023, and SC-2021, we observe distinct differences in the temperature evolution of lattice parameters. Both SC-2021 and SC-2023 exhibit a similar trend, with a sharp increase or decrease in lattice parameters between 140K and 110K. However, the ESRF data for SC-2021 shows a nearly linear change in the lattice parameters with temperature, which contrasts with the sharp transitions observed in SC-2023 and SC-2025.This suggests that SC-2021 does not undergo a spin crossover (SCO) transition.

Furthermore, the *b* lattice parameter in SC-2023 and SC-2025 exhibits negative thermal expansion, which might be linked to structural rearrangements associated with the SCO transition. The absence of this negative thermal expansion in SC-2021 further supports the idea that SC-2021 does not undergo an SCO transition. However, it is important to note that it is difficult to conclude the occurrence of an SCO transition based on lattice parameters alone. A clearer and more direct indicator of the SCO transition is obtained by mapping the evolution of Fe-N bond length, which we discuss in the following sections (section 4.2.5).

4.2.5 Bond Lengths

It is well known that the FeN_6 octahedron undergoes substantial structural changes during the spin transition (Létard et. al., 2003). To quantify the changes in the FeN_6 octahedron from HS to LS state, Fe-N bond lengths and distortion parameters (Σ) are calculated based on the structural refinement.

According to the literature, the Fe−N distances in the HS state are longer than those in the LS state and during the high-spin to low-spin (HS-LS) transition, the Fe−N distances are shortened by approximately 0.217 Å on average (Ichiyanagi et. al., 2006).

Within the compound investigated here, three pairs of nitrogen atoms form three distinct ligands surround the Fe^{2+} ion: the amine ligand (N_{amine}), the quinoline ligand ($N_{quinoline}$), and the thiocyanate ligand ($N_{thiocyanate}$). Structurally, among the three types of Fe-N bonds, the Fe-N_{amine} bond is the most restricted by the surrounded functional groups (see figure 26c). Thus, the nitrogen in the amine group is positioned farthest away from the iron atom, followed by the nitrogen in the quinoline group, while the nitrogen from the thiocyanate group is closest to the iron atom.

The Fe-N bond lengths (of SC-2021, SC-2023, and SC-2025) along with the assignment of Fe-N_n (n = 1, 2, …, 6) bonds are plotted in figure 26. The Fe-N_1, Fe-N_4, Fe-N_5, and Fe-N_6 bond of SC-2025 slightly shrink when the temperature decreases from 300 K to 140 K. The Fe-N_3 bond decreases slightly more in this temperature range compared to the Fe-N_1, Fe-N_4, Fe-N_5, and Fe-N_6 bond, while the Fe-N_2 bond slightly expands in the cooling process. However, these changes are much smaller than the average value for a SCO transition (Ichiyanagi et. al., 2006), which indicates that no spin transition happens from 300 K to 140 K. This result also correlates with the observations made in the magnetization measurements.

For the SC-2021 crystal, measured at the ESRF, the Fe-N bond length follows the expected trend of slight contraction with decreasing temperature. The bond lengths indicate that SC-2021 remains in the high-spin state without transitioning to the low-spin state, which is also confirmed from the magnetization measurement, where it shows only paramagnetic contribution at low temperatures.

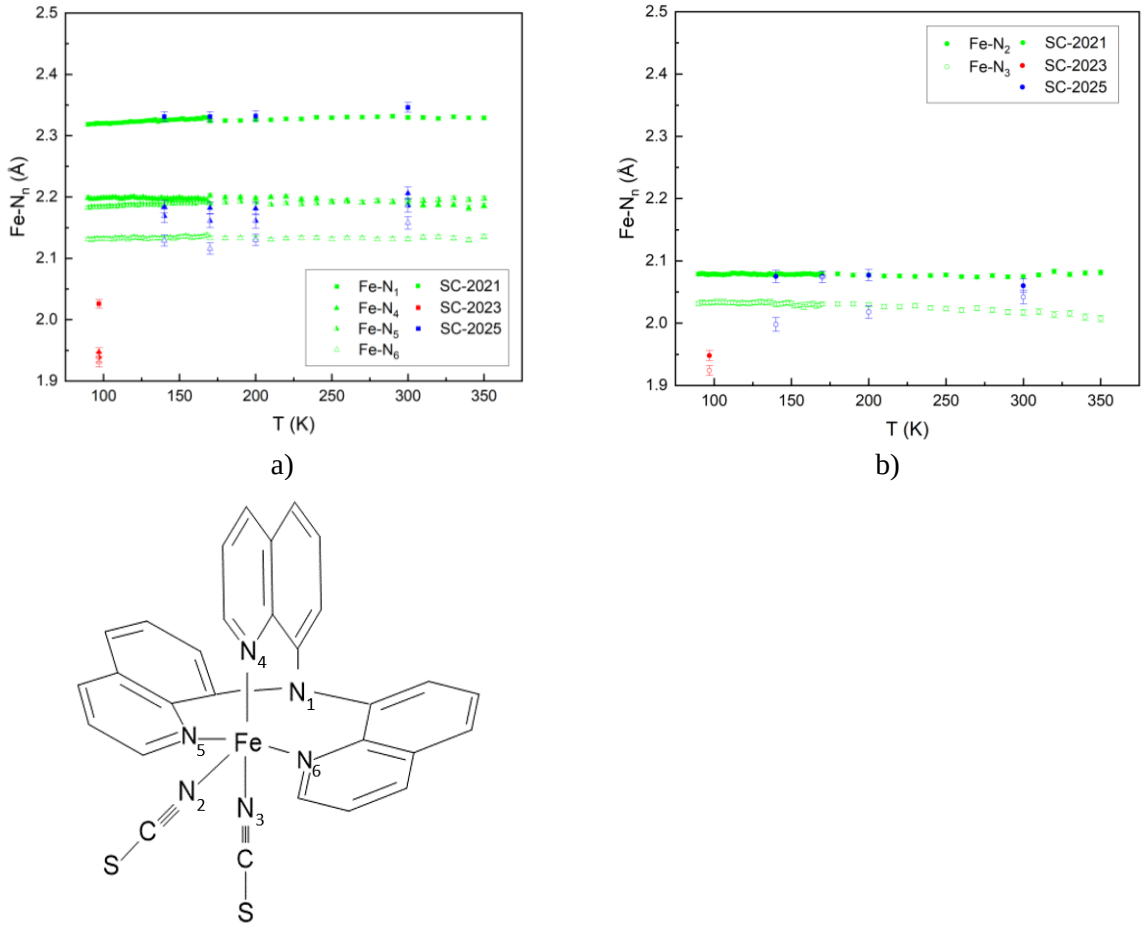

Figure 26: Comparison of Fe-N_n bond length(n = 1, 2, …, 6) between crystal SC-2021, SC-2023, and SC-2025: a) Fe-N_1, Fe-N_4, Fe-N_5, and Fe-N_6; b) Fe-N_2 and Fe-N_3; c) illustration of different Fe-N bonds in compound structure.

Looking at the dataset of SC-2023 at 97 K, all the bond lengths are much smaller than the ones in SC-2025, which indicates that the size of the FeN_6 octahedron has significantly contracted in LS state. A closer examination of the Fe-N bond lengths reveals a non-uniform contraction of the bonds associated with different ligands, where the Fe-N_{amine}, <Fe-$N_{quinoline}$> and <Fe-$N_{thiocyanate}$> exhibit a contraction of 0.32(2) Å, 0.25(1) Å and 0.12(1) Å, respectively. Despite this, the Fe-N_6 octahedra becomes more regular in the low spin state, which is also indicated by the reduced distortion parameters (see table 4 in section 4.2.3.1).

In contrast, at lower temperatures (< 140 K), one observes a clear contraction of the Fe-N bonds in the *SuperNova* data (SC-2023/SC-2025). This could be a result of the presence of solvent molecules in the compounds investigated in *SuperNova*, where the solvent is reflected in a density of approximately 5.623 $e^-/Å^3$ observed in the difference Fourier synthesis map. According to the literature, the existence of solvent molecules might hinder the freedom of structure arrangement when a compound crosses a SCO transition (Wu et. al., 2015). The solvent can strengthen the interactions between SCO centres and stabilize the crystal packing, thereby promoting a more pronounced and cooperative spin crossover behaviour.

4.2.6 Distortion Parameter

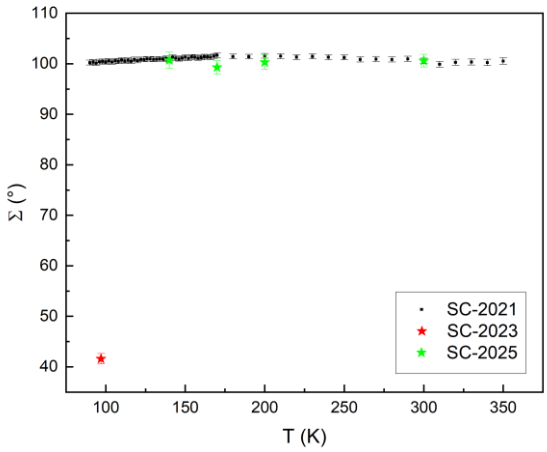

Figure 27: Comparison of distortion parameter Σ between SC-2021, SC-2023, and SC-2025

In this section we discuss the angular distortion parameter Σ, defined in section 3.5.3 for the different crystal batches studied in this thesis. As figure 27 shows, the Σ value obtained in the temperature region of the HS state (> 140 K) does not show significant variation and stays in the range between 99(1)°-101(2)°. These values correlate well with the values obtained from the ESRF data above 140 K. This is not unexpected, as both datasets correspond to the same HS spin state, making the observed similarity unsurprising. Notably, these values are relatively large compared to other spin-crossover compounds in the HS state, indicating that this compound exhibits a higher degree of distortion in its FeN_6 coordination environment (Buron-Le Cointe et. al., 2012).

The value of Σ in the LS state, listed in table 4, has been calculated from the SC-2023 and SC-2025 dataset. We observe a significant reduction in the Σ value, changing from 101(2)° to 42(1)° across the SCO, pointing towards a more ideal octahedra in the LS state. The change in the value of Σ in our case ($\Delta\Sigma$ = 59.0(1)°) appears to be much larger than the values reported in literature for other SCO compounds, such as $Fe(Pm\text{-}Bia)_2(NCS)_2$ ($\Delta\Sigma$ = 40.0(2)°) (Buron-Le Cointe et. al., 2012) and $Fe(tpa)(NCS)_2$ ($\Delta\Sigma$ = 47.8(1)°) (Li et. al., 2010).

5 Conclusion and Outlook

5.1 Conclusion

Based on the magnetic and crystallographic investigations of the compound $Fe(NQu_3)(NCS)_2 \cdot 0.5\ Et_2O$, several conclusions can be drawn.

1) The single crystal samples SC-2023/SC-2025 of $Fe(NQu_3)(NCS)_2 \cdot 0.5\ Et_2O$ exhibits an abrupt spin-crossover transition with a large thermal hysteresis, showing a transition temperature of $T_{1/2}^{\downarrow}$ = 138 K and $T_{1/2}^{\uparrow}$ = 162.5 K.

   With decreasing scan rates, the transition temperature shifts monotonically to lower temperatures and the hysteresis width continuously increases.

2) Repeated thermal cycling leads to partial degradation of the single crystal into smaller crystallites, which aligns closely with the continuous mosaicity increase of the single crystals of SC-2023/SC-2025 during the cooling process in diffraction experiments. The gradual degradation of crystallinity induces grain size effects. These effects may contribute to the observed shift in $T_{1/2}$ and the broadening of the hysteresis loop with different scan rates.

3) In the powder sample (P-2025), the temperature induced spin-crossover phenomenon is absent, which can be attributed to the lack of solvent molecules during precipitation or the easier evaporating of solvent molecules compared to single crystals. Either or both of these factors could be a potential reason for the suppression of SCO behavior in the powder samples.

4) The single crystal sample SC-2023/SC-2025 of $Fe(NQu_3)(NCS)_2 \cdot 0.5\ Et_2O$ remains in *C2/c* symmetry across the entire investigated temperature range (300 K – 95 K). At room temperature, *a* = 9.9054(2) Å, *b* = 22.3828(7) Å, *c* = 25.8754(8) Å, β = 95.5840(20)°, and V = 5709.63(45) $Å^3$. Our analysis indicates that the solvent molecules are most likely located around the special position (0.5, y, 0.25), in a cavity surrounded by aromatic rings.

5) A clear structural response to the SCO transition is observed foremost in the lattice parameters. The *a* and *c*-lattice parameters and β angle contract across the SCO, while *b*-axis expands below 140 K. The abrupt change observed in the lattice parameters between 140 K – 110 K correlates well with the sudden transition observed in the magnetization data, suggesting a strong coupling between structure and spin-state change.

6) The $Fe\text{-}N_{amine}$, $<Fe\text{-}N_{quinoline}>$ and $<Fe\text{-}N_{thiocyanate}>$ bonds exhibit a contraction of 0.32(2) Å, 0.25(1) Å and 0.12(1) Å, respectively, from 300 K to 97 K, which indicates a non-uniform contraction of FeN_6 octahedron. This bond contraction is a clear structural signature of the spin-crossover transition from the high-spin (HS) to the low-spin (LS) state. The FeN_6 octahedron in the LS state is significantly less distorted than in the HS state, as evidenced by the reduction in the distortion parameter by approximately 58%.

7) The SCO-active (SC-2023/SC-2025) crystal shows abrupt and non-linear changes in lattice parameters and a distinct contraction in $Fe–N_6$ bond lengths, highlighting the

structural response to the spin-state change. In contrast, the crystal that does not exhibit SCO (SC-2021) displays a nearly linear and gradual contraction of the lattice parameters upon cooling, with no abrupt structural rearrangements.

The crystal SC-2021, which shows no SCO transition, lacks solvent atom positions, does not exhibit an increase in mosaicity at low temperature and does not undergo the significant FeN_6 octahedral contraction or change in the distortion. These observations suggest that the presence of solvent molecules is crucial in enabling the SCO transition and the associated structural transformations.

5.2 Future Prospects

The work carried out in this thesis serves to address the complex role of solvents in the SCO nature of the compound $Fe(NQu_3)(NCS)_2 \cdot 0.5\ Et_2O$. For a more comprehensive understanding of the problem, several suggestions are made below which should be considered in future work:

1) Synchrotron based SCXRD:

   Collecting high resolution data on a single crystal at several temperature points across the SCO transition could lead to a better understanding of the distribution of solvent molecules. Additionally, one could also study the temperature evolution of inter and intra molecular interactions across the SCO. These measurements have already been carried out by our group and the data is at present being analysed.

2) Spectroscopic Investigation:

   Standard organic molecules have well defined and documented Infrared absorption bands. Thus, carrying out Infrared spectroscopic measurements could also serve as a useful tool to identify the solvent molecules in these compounds. One could also study the spin-state transition and phonon coupling from these measurements.

3) Thermo-Gravimetric Study:

   By simultaneously heating the single crystals, which exhibit a SCO, and measuring their weight, one could monitor the changes in the mass of the sample and thus obtain more detailed information on the solvent molecule.

One could further take the study ahead by (i) examining the role of different solvent molecules (ii) modifying the NCS^- branch to $NCSe^-$ and $NCBH_3$, to tailor the intermolecular interactions, and (iii) studying the modification of entropic behaviour across the spin-state transition with different solvent molecules.

Reference

Bousseksou, A., Molnár, G., Demont, P., & Menegotto, J. (2003). Observation of a thermal hysteresis loop in the dielectric constant of spin crossover complexes: towards molecular memory devices. *Journal of Materials Chemistry*, 13(9), 2069-2071.

Branders, M., & Piessens, R. (1971). Gaussian quadrature formulas for integrals with logarithmic singularity. Leuven.

Bulusu, G., & Desiraju, G. R. (2020). Strong and weak hydrogen bonds in protein–ligand recognition. *Journal of the Indian Institute of Science*, 100(1), 31-41.

Burns, R. G. (1993). *Mineralogical applications of crystal field theory* (No. 5). Cambridge university press.

Buron-Le Cointe, M. et. al. (2012). Intermolecular control of thermoswitching and photoswitching phenomena in two spin-crossover polymorphs. *Physical Review B—Condensed Matter and Materials Physics*, 85(6), 064114.

Chen, X. Q., Cai, Y. de, Ye, Y. S., Tong, M. L., & Bao, X. (2019). Investigation of SCO property-structural relationships in a family of mononuclear Fe(ii) complexes. *Inorganic Chemistry Frontiers*, 6(8), 2194–2199.

Cini, M. (2018). *Elements of Classical and Quantum Physics*. Springer International Publishing.

Delgado, T., Tissot, A., Guénée, L., et. al. (2018). Very long-lived photogenerated high-spin phase of a multistable spin-crossover molecular material. *Journal of the American Chemical Society*, 140(40), 12870-12876.

Douglas, B. Eugene., & Hollingsworth, C. A. (1985). Symmetry in bonding and spectra: an introduction. *Academic Press*.

Fagaly, R. L. (2006). Superconducting quantum interference device instruments and applications. *Review of scientific instruments*, 77(10).

Fumanal, M., Jiménez-Grávalos, F., Ribas-Arino, J., & Vela, S. (2017). Lattice-Solvent Effects in the Spin-Crossover of an Fe(II)-Based Material. the Key Role of Intermolecular Interactions between Solvent Molecules. *Inorganic Chemistry*, *56*(8), 4474–4483.

Grabowski, S. J. (Ed.). (2006). *Hydrogen bonding: new insights* (Vol. 3). Dordrecht: Springer.

Granier, T., Gallois, B., Gaultier, J., Reai, J.-A., & Zarembowitch, J. (1993). High-Pressure Single-Crystal X-ray Diffraction Study of Two Spin-Crossover Iron(II) Complexes: $Fe(Phen)_2(NCS)_2$ and $Fe(Btz)_2(NCS)_2$. In *Inorganic Chemistry* (Vol. 32).

Gütlich, P. (2013). Spin crossover - Quo vadis? *European Journal of Inorganic Chemistry*, 5–6, 581–591.

Gütlich, P., Garcia, Y., & Goodwin, H. A. (2000). Spin crossover phenomena in Fe (ii) complexesDedicated to Professor FA Cotton on occasion of his 70th birthday. *Chemical Society Reviews*, 29(6), 419-427.

Gütlich, P., & Goodwin, H. A. (2004). Spin crossover—an overall perspective. *Spin Crossover in Transition Metal Compounds I*, 1-47.

Guionneau, P., Lakhloufi, S., Lemée-Cailleau, M. H., Chastanet, G., Rosa, P., Mauriac, C., & Létard, J. F. (2012). Mosaicity and structural fatigability of a gradual spin-crossover single crystal. *Chemical Physics Letters*, 542, 52-55.

Guionneau, P., Létard, J. F., et. al. (1999). Structural approach of the features of the spin crossover transition in iron (II) compounds. *Journal of Materials Chemistry*, 9(4), 985-994.

Griffith, J. S., & Orgel, L. E. (1957). Ligand-field theory. *Quarterly Reviews, Chemical Society*, 11(4), 381-393.

Hermann, J., DiStasio Jr, R. A., & Tkatchenko, A. (2017). First-principles models for van der Waals interactions in molecules and materials: Concepts, theory, and applications. *Chemical Reviews*, 117(6), 4714-4758.

House, J. E. (2013). *Inorganic Chemistry* (pp. 201–242). Elsevier.

Huang, W., Shen, F., Zhang, M., Wu, D., Pan, F., & Sato, O. (2016). Room-temperature switching of magnetic hysteresis by reversible single-crystal-to-single-crystal solvent exchange in imidazole-inspired Fe(II) complexes. *Dalton Transactions*, 45(38), 14911–14918.

Hüppe, H. M. (2023). *Coordination Chemistry of Bioinspired Iron Complexes with Tri- and Tetradentate Ligands*. PhD thesis, RWTH Aachen.

Hunter, Christopher A., and Jeremy KM Sanders (1990). The nature of π-π interactions. *Journal of the American Chemical Society*. 112.14: 5525-5534.

Ichiyanagi, K., Hebert, J., Toupet, L., Cailleau, H., Collet, E., Guionneau, P., & Létard, J. F. (2006). Structural investigation of the photoinduced spin transition in the [Fe(PM-BiA)$_2$(NCS)$_2$] compound. *Solid State Phenomena*, 112, 81–88.

Israelachvili, J. N. (1974). The nature of van der Waals forces. *Contemporary Physics*, 15(2), 159–178.

Jabłoński, M. (2023). *Hydrogen Bonds. Molecules*, 28(4), 1616.

Jabłoński, M. (2021). Intramolecular hydrogen bonding 2021. *Molecules*, 26(20), 6319.

Jeffrey, G. A., & Yeon, Y. (1986). The Correlation Between Hydrogen-Bond Lengths and Proton Chemical Shifts in Crystals. *Acta Crystallographica*, B42, 410–413.

Jutzi, P. (1975). New Element-Carbon (p-p)$_\pi$ Bonds. *Angewandte Chemie International Edition in English*, 14(4), 232-245.

Kato, M., & Ishii, K. (2023). *Soft crystals: Flexible response systems with high structural order* (p. 265). Springer Nature.

Kittel, C., & McEuen, P. (2018). *Introduction to solid state physics*. John Wiley & Sons.

Kläui, W., Eberspach, W., & Gütlich, P. (1987). Spin-crossover cobalt (III) complexes: steric and electronic control of spin state. *Inorganic Chemistry*, 26(24), 3977-3982.

Ksenofontov, V., Levchenko, G., Spiering, H., Gütlich, P., Létard, J. F., Bouhedja, Y., & Kahn, O. (1998). Spin crossover behavior under pressure of Fe (PM-L)$_2$(NCS)$_2$ compounds with substituted 2′-pyridylmethylene 4-anilino ligands. *Chemical Physics Letters*, 294(6), 545-553.

Lakhloufi, S., Tailleur, E., Guo, W., Le Gac, F., Marchivie, M., Lemée-Cailleau, M. H., ... & Guionneau, P. (2018). Mosaicity of spin-crossover crystals. *Crystals*, 8(9), 363.

Létard, J. F., Chastanet, G., Nguyen, O., Marcén, S., Marchivie, M., Guionneau, P., Chasseau, D., & Gütlich, P. (2003). Spin Crossover Properties of the [Fe(PM-BiA)$_2$(NCS)$_2$] Complex - Phases I and II. In *Monatshefte fur Chemie* (Vol. 134, Issue 2, pp. 165–182).

Li, B., Wei, R. J., Tao, J., Huang, R. B., Zheng, L. S., & Zheng, Z. (2010). Solvent-induced transformation of single crystals of a spin-crossover (SCO) compound to single crystals with two distinct SCO centers. *Journal of the American Chemical Society*, 132(5), 1558-1566.

Liptrot, D. J., & Power, P. P. (2017). London dispersion forces in sterically crowded inorganic and organometallic molecules. *Nature Reviews Chemistry*, 1(1), 0004.

Marchivie, M., Guionneau, P., Ëois, J.-F., Âtard, L., & Chasseau, D. (2003). Towards direct correlations between spin-crossover and structural features in iron(II) complexes. *Acta Crystallographica*, 59, 479–486.

Moya, X., Kar-Narayan, S., & Mathur, N. D. (2014). Caloric materials near ferroic phase transitions. In *Nature Materials* (Vol. 13, Issue 5, pp. 439–450). Nature Publishing Group.

Milburn, G. H. W. (1973). *X-ray crystallography: an introduction to the theory and practice of single-crystal structure analysis*. London, Butterworths.

Miller, R. G., Narayanaswamy, S., Tallon, J. L., & Brooker, S. (2014). Spin crossover with thermal hysteresis in cobalt (II) complexes and the importance of scan rate. *New Journal of Chemistry*, 38(5), 1932-1941.

Miller, S. J. (2006). *The method of least squares*. Mathematics Department Brown University, 8(1), 5-11.

Muller, U. (2007). *Inorganic structural chemistry*. John Wiley & Sons (p 45-50).

Nicolazzi, W., & Bousseksou, A. (2018). Thermodynamical aspects of the spin crossover phenomenon. In *Comptes Rendus Chimie* (Vol. 21, Issue 12, pp. 1060–1074). Elsevier Masson SAS.

Palatinus, L., & Chapuis, G. (2007). SUPERFLIP - A computer program for the solution of crystal structures by charge flipping in arbitrary dimensions. *Journal of Applied Crystallography*, 40(4), 786–790.

Palatinus, L. (2013). The charge-flipping algorithm in crystallography. Acta Crystallographica Section B: Structural Science, *Crystal Engineering and Materials*, 69(1), 1–16.

Petříček, V., Dušek, M., & Palatinus, L. (2014). Crystallographic computing system JANA2006: general features. *Zeitschrift für Kristallographie-Crystalline Materials*, 229(5), 345-352.

Petříček, V., Palatinus, L., Plášil, J., & Dušek, M. (2023). Jana2020–a new version of the crystallographic computing system Jana. Zeitschrift für Kristallographie-Crystalline Materials, 238(7-8), 271-282.

Phonsri, W., Harding, P., Liu, L., Telfer, S. G., Murray, K. S., Moubaraki, B., Ross, T. M., Jameson, G. N. L., & Harding, D. J. (2017). Solvent modified spin crossover in an iron(III) complex: Phase changes and an exceptionally wide hysteresis. *Chemical Science*, 8(5), 3949–3959.

Planes, A., Stern-Taulats, E., Castán, T., Vives, E., Mañosa, L., & Saxena, A. (2015). Caloric and multicaloric effects in shape memory alloys. *Materials Today: Proceedings*, 2, S477-S484.

Pillai, S. O. (2006). *Solid state physics*. New Age International.

Quantum Design, Inc. PPMS DynaCool – Product Description, 2019. https://www.qdusa.com/products/dynacool.html (access on 18.03.2025)

Rossmann, M.G., Arnold, E. (2006). Patterson and molecular-replacement techniques. In *International Tables for Crystallography*. Vol.B, pp. 235-263.

Šalitroš, I., Fuhr, O., & Ruben, M. (2016). Solvent-induced polymorphism of iron(II) spin crossover complexes. *Materials*, 9(7).

Sanderson, R. (2012). *Chemical bonds and bonds energy* (Vol. 21). Elsevier. (pp. 75)

Scepaniak, J. J., Harris, T. D., Vogel, C. S., Sutter, J., Meyer, K., & Smith, J. M. (2011). Spin crossover in a four-coordinate iron (II) complex. *Journal of the American Chemical Society*, 133(11), 3824-3827.

Schenk, H., University of Wales (Cardiff), Union internationale de cristallographie. Commission on Crystallographic Teaching, & Taylor, C. A. (1984). *An introduction to direct methods: the most important phase relationships and their application in solving the phase problem*. International Union of Crystallography.

Schwarzenbach, D. (1996). *Crystallography*. John Wiley & Sons

Shahed, H. S. A. R. (2024). *Elucidation of Barocaloric Effect in Spin Crossover Compounds*. PhD thesis, Forschungszentrum Jülich GmbH.

Shannon, R. D. (1976). Revised Effective Ionic Radii and Systematic Studies of Interatomie Distances in Halides and Chaleogenides. In *Acta Cryst* (Vol. 32).

Shatruk, M., Phan, H., Chrisostomo, B. A., & Suleimenova, A. (2015). Symmetry-breaking structural phase transitions in spin crossover complexes. *Coordination Chemistry Reviews*, 289, 62-73.

Sheldrick, G. M., Gilmore, C. J., Hauptman, H. A., Weeks, C. M., Miller, R., & Usón, I. (2012). SUPERFLIP: charge flipping. *International Tables for Crystallography*. Vol. F. ch. 16.1, pp. 428-429.

Siddiqui, S. A., Domanov, O., Schafler, E., Vejpravova, J., & Shiozawa, H. (2021). Synthesis and size-dependent spin crossover of coordination polymer $[Fe(Htrz)_2(trz)](BF_4)$. *Journal of Materials Chemistry C*, 9(3), 1077–1084.

Siegrist, Theo. 2021, *X-Ray Structure Analysis*. Walter de Gruyter GmbH & Co KG.

Steiner, T. (2002). The hydrogen bond in the solid state. *Angewandte Chemie International Edition*, 41(1), 48-76.

Stout, G. H., & Jensen, L. H. (1989). *X-ray structure determination: a practical guide*. John Wiley & Sons.

Sun, X. P., Wei, R. J., Yao, Z. S., & Tao, J. (2018). Solvent Effects on the Structural Packing and Spin-Crossover Properties of a Mononuclear Iron(II) Complex. *Crystal Growth and Design*, 18(11), 6853–6862.

Traiche, R., Sy, M., Oubouchou, H., Bouchez, G., Varret, F., & Boukheddaden, K. (2017). Spatiotemporal observation and modeling of remarkable temperature scan rate effects on the thermal hysteresis in a spin-crossover single crystal. *The Journal of Physical Chemistry C*, 121(21), 11700-11708.

Urland, W., & Niketić, S. R. (1986). Failure of crystal field theory: an example. *Chemical physics letters*, 129(6), 592-594.

Valls, Robert. (2018). *Inorganic Chemistry*. Wiley-ISTE [Imprint] John Wiley & Sons, Incorporated. (pp. 54-55, 124-125)

van Beek, W., Safonova, O. V., Wiker, G., & Emerich, H. (2011). SNBL, a dedicated beamline for combined in situ X-ray diffraction, X-ray absorption and Raman scattering experiments. *Phase Transitions*, 84(8), 726-732.

Van der Sluis, P. V., & Spek, A. L. (1990). BYPASS: an effective method for the refinement of crystal structures containing disordered solvent regions. *Foundations of Crystallography*, 46(3), 194-201.

Van Koningsbruggen, P. J., Maeda, Y., & Oshio, H. (2004). Iron (III) spin crossover compounds. *Spin crossover in transition metal compounds I*, 259-324.

Vela, S., & Paulsen, H. (2018). Cooperativity in Spin Crossover Systems. An Atomistic Perspective on the Devil's Staircase. *Inorganic Chemistry*, 57(15), 9478–9488.

Von Ranke, P. J., Alho, B. P., Nobrega, E. P., Caldas, A., de Sousa, V. S. R., Colaço, M. v., Marques, L. F., Rocha, G. M., Rocco, D. L., & Ribeiro, P. O. (2019). The refrigerant capacity in spin-crossover materials: Application to $[Fe(phen)_2(NCS)_2]$. *Journal of Magnetism and Magnetic Materials*, 489.

Wong-Ng, W. et. al., (2001). Standard reference material (SRM 1990) for single crystal diffractometer alignment. *Journal of research of the National Institute of Standards and Technology*, 106(6), 1071.

Wu, X. R., Shi, H. Y., Wei, R. J., Li, J., Zheng, L. S., & Tao, J. (2015). Coligand and solvent effects on the architectures and spin-crossover properties of (4, 4)-connected Iron (II) coordination polymers. *Inorganic Chemistry*, 54(8), 3773-3780.